Earthquake Research Advances xxx (xxxx) xxx

Contents lists available at ScienceDirect

Earthquake Research Advances

journal homepage: www.keaipublishing.com/en/journals/earthquake-research-advances

Foreshock behaviors and mainshock rupture properties associated with the 2025 M_W 8.8 Kamchatka earthquake sequence

Phuc Mach[a,*], Xu Si[a], Dun Wang[b], Robert Shcherbakov[c], Ping He[b], Tuncay Taymaz[d,e], Chang Ding[a], Zhigang Peng[a]

[a] School of Earth and Atmospheric Sciences, Georgia Institute of Technology, Atlanta, GA 30332, USA
[b] Chinese University of Geosciences, Wuhan, Hubei 430074, China
[c] Department of Earth Sciences, Western University, London, Ontario 54901, Canada
[d] Department of Geophysical Engineering, İstanbul Technical University, ITU Ayazaga Campus, Maslak, Sarıyer, TR-34469, İstanbul, Türkiye
[e] Disaster Management Institute, İstanbul Technical University, ITU Ayazaga Campus, Maslak, Sarıyer, TR-34469, İstanbul, Türkiye

ARTICLE INFO

Keywords:
Kamchatka
Foreshock
Aftershock
Back projection
Afterslip
Megathrust earthquake

ABSTRACT

The July 29, 2025 M_W 8.8 Kamchatka earthquake ruptured the plate interface off the east coast of the Kamchatka Peninsula along the Kuril-Kamchatka subduction zone and generated tsunamis across the Pacific Ocean, followed by volcanic eruptions in Kamchatka. The mainshock was preceded by an energetic foreshock sequence that began with a M_W 7.4 event on July 20, 2025, located 40 km northeast of the mainshock hypocenter. However, the physical mechanisms connecting the foreshock to the mainshock are not completely clear. In this study, we present a detailed seismological and geodetic analysis of the sequence by investigating the rupture characteristics of the M_W 8.8 mainshock, the spatiotemporal evolution of the foreshock and early aftershock sequence, and the processes driving their interaction. Teleseismic back projection reveals that the mainshock ruptured predominantly toward the southwest with a total source duration of ~220 s. The M_W 7.4 foreshock was accompanied by afterslip along the plate interface, which likely drove an expanding aftershock of its own and eventually triggered the mainshock nucleation. This event also shows anomalously high aftershock productivity relative to other Mbl7+ events before and after the mainshock, indicating an elevated likelihood of triggering a larger earthquake. We also identify possible segmentation of the megathrust rupture zone along the Kuril-Kamchatka subduction zone that is separated by higher topography in the upper plate. These results provide new insight into the physical mechanisms of foreshocks and segmentation of mainshock ruptures along major subduction zones, with direct implications for short-term forecasting and seismic hazard assessment of megathrust earthquakes in this and other regions.

1. Introduction

On July 29, 2025, at 23:24:52 UTC, a moment magnitude (M_W) 8.8 earthquake occurred off the east coast of the Kamchatka Peninsula (Fig. 1). The event occurred in the Kuril-Kamchatka subduction zone, one of the most seismically active plate boundaries around the Pacific Rim. This plate interface has hosted multiple large interplate earthquakes during the past century, including a M_W 8.8-9.0 event on November 4, 1952 (Johnson and Satake, 1999; MacInnes et al., 2010; Bilek and Lay, 2018). This 2025 M_W 8.8 mainshock ruptured a similar

* Corresponding author.
E-mail addresses: pmach3@gatech.edu (P. Mach), xsi33@gatech.edu (X. Si), wangdun@cug.edu.cn (D. Wang), rshcherb@uwo.ca (R. Shcherbakov), phe@cug.edu.cn (P. He), taymaz@itu.edu.tr (T. Taymaz), cding64@gatech.edu (C. Ding), zpeng@gatech.edu (Z. Peng).

Peer review under the responsibility of Editorial Board of Earthquake Research Advances.

Production and Hosting by Elsevier on behalf of KeAi

https://doi.org/10.1016/j.eqrea.2026.100457
Received 22 November 2025; Received in revised form 19 February 2026; Accepted 10 March 2026

Please cite this article as: Mach, P. et al., Foreshock behaviors and mainshock rupture properties associated with the 2025 M_w 8.8 Kamchatka earthquake sequence, Earthquake Research Advances, https://doi.org/10.1016/j.eqrea.2026.100457

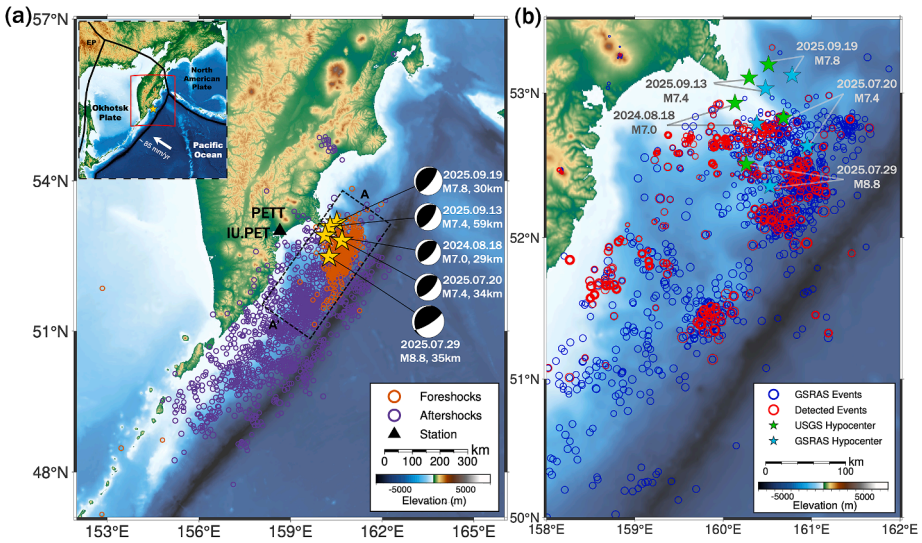

Fig. 1. (a) Map view of the M 8.8 Kamchatka earthquake with 10 days of foreshocks (orange), 10 days of aftershocks (purple) and focal mechanism (with magnitude and depth) of the $M_w \geq 7.0$ events. A-A′ profile presenting the trench-parallel distance in Fig. 5b. (b) Map view of the local catalog events (blue) from the Geophysical Survey of the Russian Academy of Sciences (GSRAS) and template-matching detected events (red) with the location of the $M_W \geq 7.0$ events in USGS and GSRAS catalogs.

patch and was preceded by a foreshock sequence that started on July 20, with the latest event being a M_W 7.4 event (Bradley and Hubbard, 2025a; Hubbard and Bradley, 2025a; Stein et al., 2025). The foreshock event occurred close to the mainshock hypocenter, and its productivity appeared to be higher than other M_W 7+ events that occurred before and after the M_W 8.8 mainshock (Stein et al., 2025). Long-term monitoring in Kamchatka has shown that multiple independent precursor signals often emerge prior to large megathrust earthquakes and before more frequent as rupture approaches, reflecting progressive physical preparation of the fault before failure (Kopylova et al., 2025).

It is worth noting that a smaller M_W 7.0 earthquake occurred near the hypocenter of the M_W 7.4 event on August 17, 2024, but was not followed by a larger event (Bradley and Hubbard, 2024; Chebrov et al., 2025). This highlights the difficulty of using elevated seismicity alone (i.e., foreshocks) as a harbinger for larger earthquakes (Peng and Lei, 2025). In other regions such as the Japan Trench and northern Chile, recent studies showed elevated foreshock rates, migrating seismicity, and short-term slow slip before some large events (Kato et al., 2012; Ruiz et al., 2014), whereas other large earthquakes show little or no clear pre-seismic deformation or precursory signals (Roeloffs, 2006; Peng and Lei, 2025).

With high-resolution earthquake catalogs and geodetic observations, there is a renewed interest in studying foreshock activity and short-term aseismic transients relating to the nucleation of the mainshock around the world (Beroza et al., 2021; Zhou et al., 2022; Wang et al., 2024, 2025; Bletery and Nocquet, 2023, 2025; Bradley and Hubbard, 2024; Martínez-Garzón and Poli, 2024; Peng and Lei, 2025; Lippiello et al., 2025; Rodkin et al., 2025; Goltz, 2025). In this study, we assemble a unified seismological and geodetic dataset of the 2025 Kamchatka sequence to characterize its preseismic evolution and coseismic rupture. We integrate teleseismic back-projection of P waves to image the mainshock ruptures, and a single-station template-matching detection to enrich the catalogs of foreshocks and the earliest aftershocks. Using these tools, we quantify the statistical behavior before and after the mainshock, map the timing and migration of high-frequency radiation during the mainshock rupture, and delineate the geometry, segmentation, and depth extent of the mainshock slip on the plate interface. We combine the seismological dataset with GNSS recordings to observe aseismic transients before the mainshock. We also complement the seismic analysis with available InSAR images to place constraints on the onshore displacement and track the onset of early post-seismic deformation. In addition, we examine potential segmentations of megathrust ruptures in the study region.

2. Tectonic background and the initial observations of the *M* 8.8 mainshock

The Kamchatka Peninsula is at the northern section of the 2100-km Kuril-Kamchatka arc (Fig. 1), where the Pacific plate subducts beneath the Okhotsk microplate, forming an island chain along the arc, a continuous volcanic front, and the deep Kuril-Kamchatka Trench (Ruppert et al., 2007). The plate convergence near the 2025 mainshock rupture is rapid and directed to the northwest, with rates estimated to be 80 mm/yr (DeMets et al., 2010). This plate convergence shows a variety in obliquity with the deformation south of the Kamchatka peninsula partitioned into thrust motion on the megathrust and a small part of strike slip in the forearc, while the north toward Kamchatka becomes more trench normal (Ruppert et al., 2007; Kozhurin and Zelenin, 2017). The Wadati-Benioff zone is well defined, and the slab dip shallows under the influence of the Meiji Seamount chain and the Aleutian transform (Hayes et al., 2018).

In this region, the earthquake productivity is among the highest worldwide, with megathrust earthquakes occurring near the trench down to the depths of 40-60 km, and intermediate-depth to deep-focus earthquakes up to 600-700 km in the Sea of Okhotsk (Zhan et al., 2014). Historic aftershock zones of large events have been used to infer segmented behavior and to define seismic gaps. For example, the 2006–2007 central Kuril sequence started with a M_W 8.3 earthquake in November 2006 that ruptured a long-standing gap, followed by a M_W 8.1 outer rise normal faulting event in January 2007 (Ammon et al., 2008), forming a notable doublet. The 2025 event took place in a region that was also ruptured during the 1952 M 8.8-9.0 event, which had a devastating tsunami impact (Johnson and Satake, 1999; MacInnes et al., 2010). However, finite-fault slip inversions from teleseismic and geodetic observations show that the ruptures of the 1952 and 2025 events appear to complement each other, with the 2025 rupture likely reactivating parts of the 1952 megathrust rupture at greater down-dip depths and showing minimal near-trench slip (Mikhailov et al., 2025; Yagi et al., 2025; Ruiz-Angulo et al., 2025; Periollat and Funning, 2026; Liu et al., 2026).

The 2025 M_W 8.8 event is categorized as one of the ten largest earthquakes worldwide since 1900 (Bradley and Hubbard, 2025a). Based on finite-fault slip inversions, the mainshock slip-plane size was estimated to be 600 km along strike in length, by 140-175 km in width (Yin et al., 2026; Bradley and Hubbard, 2025a; Hubbard and Bradley, 2025b). The peak slip exceeded 10 m across a broad region of the mainshock rupture zone (Yagi et al., 2025; Liu et al., 2026; Ishijima and

Watada, 2026), and the total source duration was about 220 s (Xu et al., 2025; Zhou et al., 2025). The location and the focal mechanism of the mainshock are consistent with reverse faulting on the subduction interface of the Kuril-Kamchatka arc.

The 2025 earthquake generated a Pacific-wide tsunami recorded by tide gauges, deep ocean sensors, and satellite altimetry observations (Ruiz-Angulo et al., 2025), but coastal impacts were uneven. In the Northern Kuril Islands, the maximum run-up was recorded up to 19 m (Stein et al., 2025). Field surveys documented widespread coastal impacts, with run-up heights of 5 to 10 m and localized maxima exceeding 10 m to 16 m along the Kamchatka and northern Kuril coasts (Pinegina et al., 2026). The Pacific Tsunami Warning Center (PTWC) observed amplitudes of 1.74 m at Maui, Hawaii, and 1.13 m in Crescent City, California, USA. However, despite the earthquake's large magnitude and the basin-wide propagation, the observed tsunami caused only minor local and far-field impacts. Additionally, records indicate that multiple Kamchatka volcanoes were activated in the days following the mainshock, including Mount Klyuchevskoy and Mount Krasheninnikov. Mount Klyuchevskoy had its continuing and intensive eruption with lava fountains starting July 30, just hours after the mainshock, with the long ash plumes documented through mid-August (Smithsonian Global Volcanism). Mount Krasheninnikov had its first eruption after centuries of being inactive on August 2, with activity lasting about two weeks (FEB Russian Academy of Sciences, Smithsonian Global Volcanism). The temporal association between the M_W 8.8 mainshock and these eruptions is consistent with patterns discussed in prior work on earthquake-volcano interactions (Manga and Brodsky, 2006; Eggert and Walter, 2009) and calculated rock pressure changes due to the M_W 8.8 mainshock (Liu et al., 2026).

As noted before, a M_W 7.0 reverse-faulting earthquake occurred east of Petropavlovsk-Kamchatsky on August 17, 2024 (Bradley and Hubbard, 2024; Chebrov et al., 2025). However, that sequence was not followed by another larger event. On another hand, the M_W 7.4 event on July 20, 2025 occurred farther east and initiated a distinct aftershock sequence whose activity decayed with time until the 2025 moment magnitude 8.8 mainshock initiated in the southwest of the 7.4 event (Stein et al., 2025). Two large aftershocks then occurred in the northern part of the aftershock region, including a M_W 7.4 on September 13, followed by a M_W 7.8 on September 19 (Fig. 1b). These aftershocks occurred in the north of the M_W 8.8 mainshock, near the 1923 M 8.5 and 1959 M 8.2 earthquakes (Hubbard and Bradley, 2025b; Bradley and Hubbard, 2025b) just offshore of Cape Shipunskiy (Fig. 1a).

3. Mainshock rupture properties from a back-projection analysis

We first apply a P-wave back-projection method (Wang and Mori, 2011; Wang et al., 2016; Kiser and Ishii, 2017) to image the rupture process of the 2025 Kamchatka Peninsula earthquake using teleseismic data recorded by regional arrays in Europe (EU), the United States (US), and Australia (AU) (Fig. 2a). The same procedure has been applied to image the rupture extent following the 2024 M 7.5 Noto Peninsula, Japan earthquake (Peng et al., 2025b) and the 2025 M 7.7 Sagaing fault earthquake in Myanmar (Peng et al., 2025a). As was done before, the locations of the maximum energy points are plotted to highlight the primary rupture features (Fig. 2). These three arrays (EU, AU, and US) are located to the northwest, southwest, and northeast of the epicenter, respectively, with epicentral distances ranging from 30° to 90°, which is the optimal range for teleseismic P-wave back-projection (Kiser and Ishii, 2017). While the results from these arrays differ slightly, their primary features are mutually consistent: the mainshock ruptured predominantly southwestward along the subduction interface with a rupture length of approximately 500 km. The total source duration is about 220 s (the average rupture speed is ~2.3 km/s), consistent with other finite-fault inversion results (Xu et al., 2025; Zhou et al., 2025),

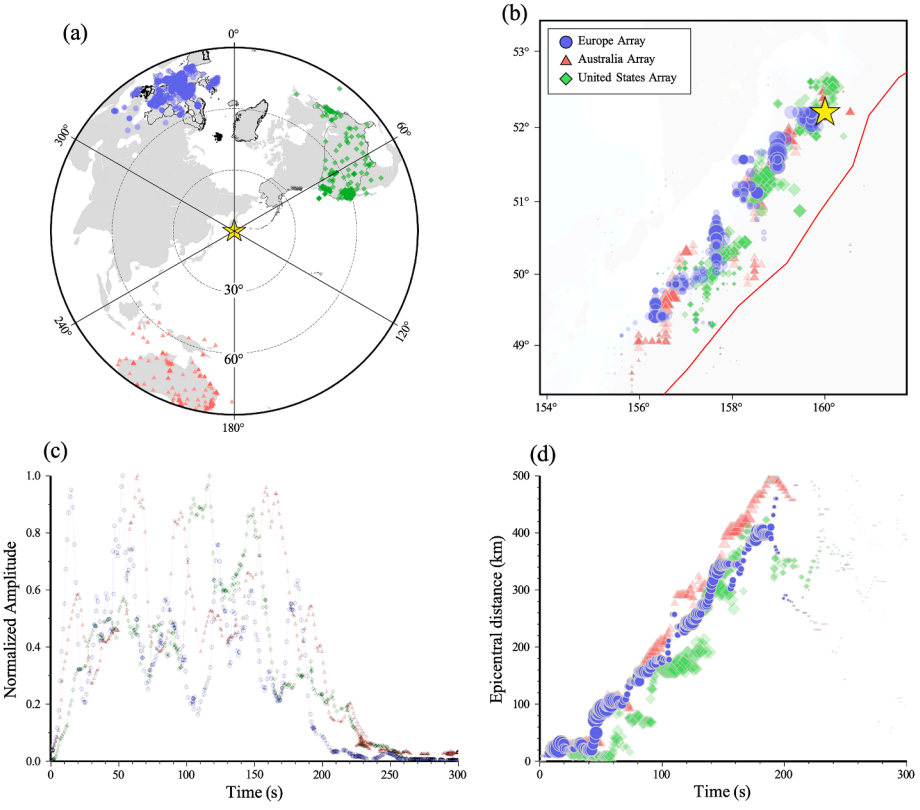

Fig. 2. Rupture imaging of the 2025 M_W 8.8 Kamchatka earthquake by back-projection. (a) Locations of seismic stations used for back-projection from the U.S. (green), European (blue), and Australian (red) seismic networks; (b) Spatiotemporal distribution of radiated energy derived from back-projection; (c) Energy–time curve of the back-projection results. (d) Time-distance plot of the back-projection results.

but slightly shorter than the interpreted duration of ~190 s by the USGS (Yin et al., 2026). However, the mainshock source functions likely contained 3-4 sub-events, illustrated as multiple separated yet continuous bursts in the time-distance distribution (Fig. 2d), and the rupture speeds were not uniform, indicating multiple peaks of high-frequency energy radiations during the mainshock.

4. InSAR data analysis

To capture the coseismic deformation field, we analyze three Sentinel-1A/C interferogram pairs: one descending pair (track 060, July 19–31, 2025) and two ascending pairs (track 111, July 23–August 4, 2025; track 038, July 18–30, 2025). Standard interferometric processing steps ensured precise image alignment and reliable phase retrieval, after which the interferograms were geocoded into the UTM projection. Atmospheric delays were corrected using GACOS products (Yu et al., 2018), which proved particularly effective in volcanic regions where steep relief commonly amplifies tropospheric phase distortions.

The unwrapped interferograms (Fig. 3) reveal pronounced coseismic deformation across the onshore Kamchatka region, despite the earthquake occurring offshore more than 100 km from the nearest coastline. Retrieved line-of-sight (LOS) displacements range from −22.7 cm to 91.9 cm for descending track 060, from −108.4 cm to 18.3 cm for ascending track 111, and from −28.8 cm to 13.6 cm for ascending track 038 (Fig. 3a–c). The deformation field is characterized by opposite LOS polarities between ascending and descending geometries, a broad spatial extent exceeding 400 km, and a smooth gradient (Fig. 3d). These features indicate that the LOS deformation was dominated by an east-west horizontal component accompanied by substantial vertical uplift, with additional contributions from north-south motion that are not explicitly resolved in the LOS geometry. This is consistent with ALOS-2 InSAR observations showing dominant eastward displacement exceeding 1.5 m and shallow megathrust slip at depths of 10 km to 20 km (Himematsu and Munekane, 2025). Such a wide and gentle deformation pattern is diagnostic of slip on a shallowly dipping offshore megathrust fault.

As noted before, the mainshock was reported to have triggered activity at seven Holocene volcanoes, including a strong eruption of Krasheninnikov (Global Volcanism Program GVP, 2025). Because the eruption of Krasheninnikov occurred several days after the mainshock, it falls outside the temporal coverage of the InSAR pairs analyzed in this study. Moreover, no clear volcanic activity–related deformation signals are detected at the other six volcanoes. In contrast, subtle deformation features are suggested at Ksudach and Opala (Fig. 3d). Overall, these findings underscore the heterogeneous nature of earthquake–volcano interactions, with only certain volcanic systems responding measurably to large subduction earthquakes (Walter and Amelung, 2007; Eggert and Walter, 2009).

5. Foreshock and aftershock patterns from local and template matching catalogs

In this section, we analyze the microseismicity before and after the mainshock from both local and global earthquake catalogs and a template-matching-based catalog. Each dataset provides different resolution and uncertainty characteristics, which are important to consider when interpreting spatial and temporal patterns. Due to the offshore source geometry and data access, continuous recordings from a single nearby broadband station IU. PET was available. A high-resolution earthquake catalog was therefore constructed by applying a single-station template matching to the continuous data. Matched-filtered detection uses waveform similarity to recover small earthquakes that original catalogs miss, which lowers the magnitude of completeness and sharpens clustering in space and time (Gibbons and Ringdal, 2006; Peng and Zhao, 2009; Yang et al., 2009; Kato et al., 2012; Ross et al., 2019). With this method, we enhance our observation of spatio-temporal evolutions of the July 20 foreshock sequence and events right after the M_W 8.8 mainshock.

To characterize the foreshock and aftershock patterns, we use multiple earthquake catalogs to analyze seismological behaviors under different location uncertainties. Specifically, we use the catalogs from the United States Geological Survey (USGS) and the local Geophysical Survey of the Russian Academy of Sciences (GSRAS). For the Kamchatka sequence, the USGS catalog is determined using a global seismic network, which provides robust detection of large offshore events but is commonly associated with significant depth uncertainty for subduction zone earthquakes. The local catalog is produced by the Kamchatka Regional Seismological Center of GSRAS, which operates a regional seismic network across the Kamchatka Peninsula (Chebrov et al., 2013; Chebrova et al., 2020). This network consists primarily of onshore

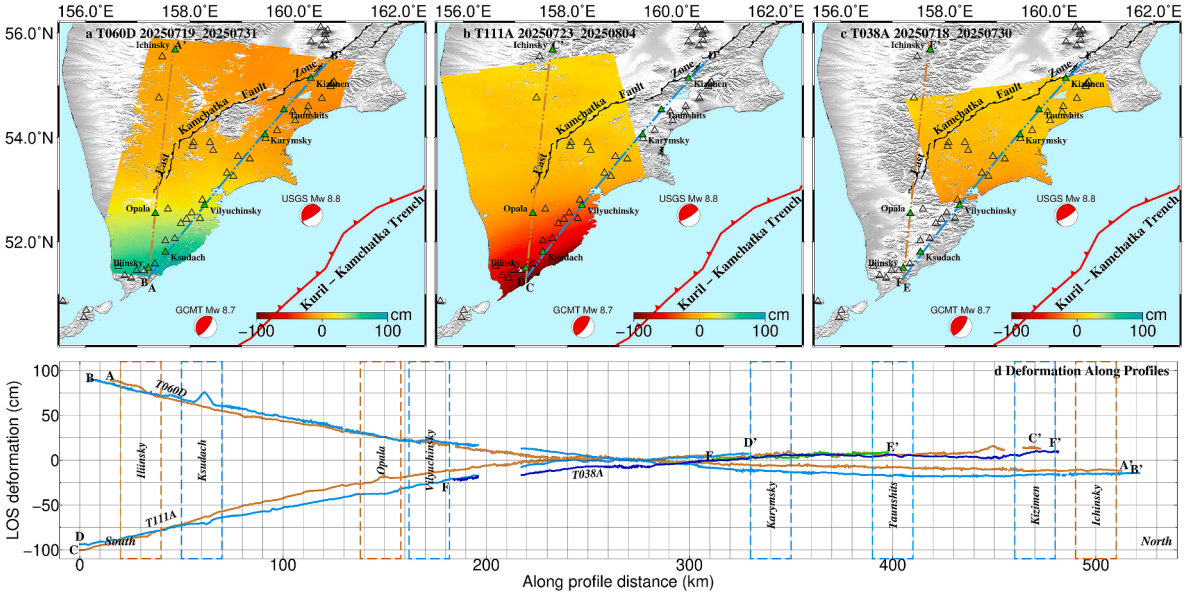

Fig. 3. Sentinel-1 interferogram of the coseismic deformation from the Kamchatka earthquake. (a)-(c) Retrieved line-of-sight for three different tracks. (d) LOS deformation field in comparison to the along-profile distance.

seismic stations, with dense coverage in central and southern Kamchatka. As a result, earthquake locations for offshore events may still be affected by hypocenter uncertainty due to station geometry, phase picking and velocity model assumptions. Event locations in the GSRAS catalog are obtained through routine regional processing using a local velocity model optimized for the Kamchatka region. In the study, we use the published catalog locations directly and interpret them as internally consistent regional solutions. An important advantage of the GSRAS catalog is its higher detection capability for small-magnitude events, providing a much denser catalog that includes microearthquakes with magnitudes as small as approximately −0.5. The overall magnitude of completeness determined using the Maximum Curvature Method +0.2 magnitude (Woessner and Wiemer, 2005) is about 1.35. This enhanced completeness is valuable for resolving short-term seismicity evolution.

Using both catalogs, a single station template matching detector was applied to recover events that were poorly recorded or absent from the original catalogs. Firstly, we extract all events recorded by station IU.PET from the local catalog, obtaining a total of 9143 events spanning August 1, 2024, to September 22, 2025. Each event is then processed using EQTransformer (Mousavi et al., 2020) for automatic phase picking, with thresholds of P_threshold = 0.1 and S_threshold = 0.1. We retain only those events that contained both P and S arrivals within the same record, resulting in 3441 qualified events. Subsequently, we apply a 1–10 Hz band-pass filter to both the continuous and template waveforms at IU.PET. For each waveform, we extract a time window extending 5 s before the P-wave arrival and 8 s after the phase arrivals. Finally, we compute the mean cross-correlation coefficients (CCCs) between the template and continuous waveforms and consider detections with CCC $\geq$ 0.7 as valid new events. This threshold roughly corresponds to the ~12 km event-separation distances, based on the 90% distribution curve with all the GSRAS template event (Fig. S3).

In total, 523 templates produced successful detections, resulting in 999 new events with mean correlation coefficients (cc) $\geq$ 0.7 during a 78-day period from 6 July to September 22, 2025, surrounding the M 8.8 mainshock. A relatively high correlation threshold was chosen, rather than a conventional median absolute deviation (MAD) criterion, to ensure the reliability of the newly detected events. Since only a single continuous station (IU.PET) was available, the detected events were assigned the hypocenters of their corresponding templates, meaning their mapped locations coincide with those templates rather than being independently relocated. Accordingly, the locations of the detected events are used to describe relative spatial and temporal patterns within the catalog, rather providing new absolute hypocentral constraints. The magnitudes of the detected events were estimated based on their relative amplitudes with respect to the templates. A tenfold increase in waveform amplitude relative to the template corresponds approximately to a one-unit increase in magnitude (Peng and Zhao, 2009). Immediately after the mainshock, early aftershocks are recovered with a match-filtered technique while still embedded in the coda. Fig. 4 shows an example of a detected early aftershock event using the matched-filter technique. The newly detected event occurred at 27 100 s (~7.5 h) following the mainshock and had an inferred magnitude of 3.9.

Fig. 1b shows GSRAS locations for the ten days of aftershocks following the M 8.8 mainshock, with template-matched detections overlaid. A systematic catalog offset is also evident, in which for events of magnitude 7.0 and larger, USGS epicenters plot consistently to the northwest, approximately 40 km, of the corresponding GSRAS solutions (Fig. 1b). This difference likely reflects distinct networks or velocity models and is noted when interpreting spatial patterns. Our conclusions are based on relative distributions within each catalog rather than on absolute epicentral agreement.

When events are viewed in trench-parallel coordinates along the Kamchatka-Kuril plate interface (Fig. 5), foreshock activity beginning around the M_W 7.4 event is found to concentrate near the M_W 8.8 mainshock hypocentral region, with additional clusters distributed along the plate interface. In the first 20 h after the M_W 7.4 event, detected events are concentrated in both northern and southern areas of the event, and the activity remains close to the hypocentral area. From

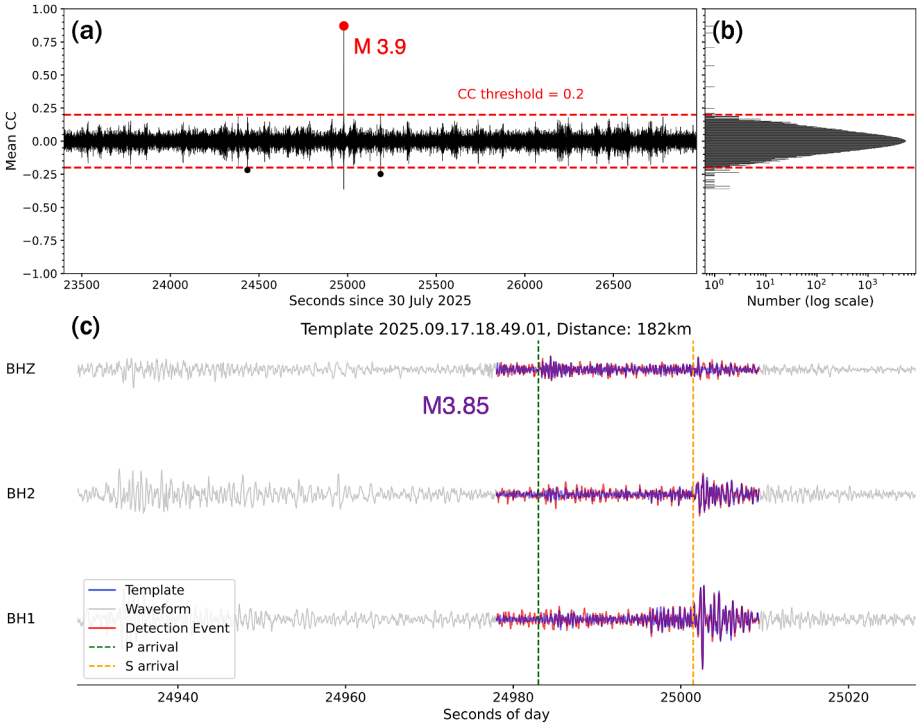

Fig. 4. Example of a detected early aftershock. (a) Mean cross-correlation (CC) functions for the template event 20250917184901. The black dots are detections exceeding the absolute threshold (red dashed line), and the red dot corresponds to the detected M 3.90 event matched with the M 3.85 template. (b) The histogram of the mean correlation coefficient functions. (c) A comparison of the template waveforms (red) and the continuous waveforms (grey).

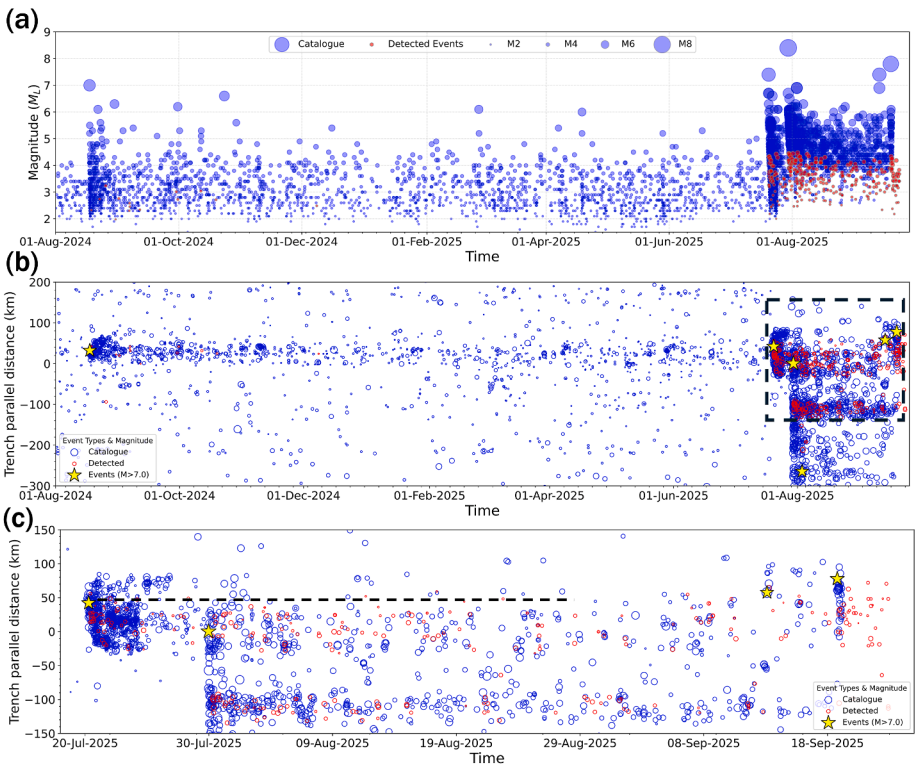

Fig. 5. Observation of the Kamchatka sequence in the trench parallel distance. (a) The magnitude frequency distribution from August 1, 2024 to September 25, 2025. (b) Earthquake migration toward the rupture initiation point of the mainshock. Space-time diagram of all local catalogue events and detected events between August 1, 2024 and September 23, 2025, with earthquake origin locations indicated in terms of the distance along the trench axis (the width of the profile is 100 km, demonstrated as A-A′ profile in Fig. 1a). (c) Zoomed in on the smaller area of the sequence in Fig. b (black box). The aftershocks of the *M* 8.8 event, starting from August 20, 2025 to September 23, 2025, included the *M* 7.4 aftershock and *M* 7.8 aftershock.

July 21 to 28, 2025, the foreshock distribution broadened mainly along strike toward the southwest while remaining confined in trench normal distance (Fig. 5).

The aftershocks following the *M* 7.4 foreshock appear to show systematic migrations aligned with the trench parallel direction (Fig. 5c). To further quantify their migration patterns, we attempt to fit the seismicity front with two spatial migration functions: sqrt(t) for fluid-driven seismicity (Shapiro et al., 1997; Sheng et al., 2022; Lei et al., 2024), and log10(t) for afterslip-driven seismicity (Peng and Zhao, 2009; Ross et al., 2017; Perfettini et al., 2018). Both fits capture a clear decelerating expansion of activity ($R^2 \approx 0.67$ for $\sqrt{t}$ and $R^2 \approx 0.80$ for $\log_{10}(t)$; Fig. 6c and d), suggesting a systematic migration of seismicity with time. These fitted migration curves depend on the underlying earthquake locations and may be influenced by systematic location uncertainties. Hence, we emphasize the relative temporal evolution and the overall decelerating pattern rather than the exact fitted migration distances. From Fig. 6c–d, the aftershock expansion front is reasonably fit by both $\sqrt{t}$ and $\log_{10}(t)$ models, with the corresponding relations as $R = -0.09\sqrt{t} + 19.68$ or

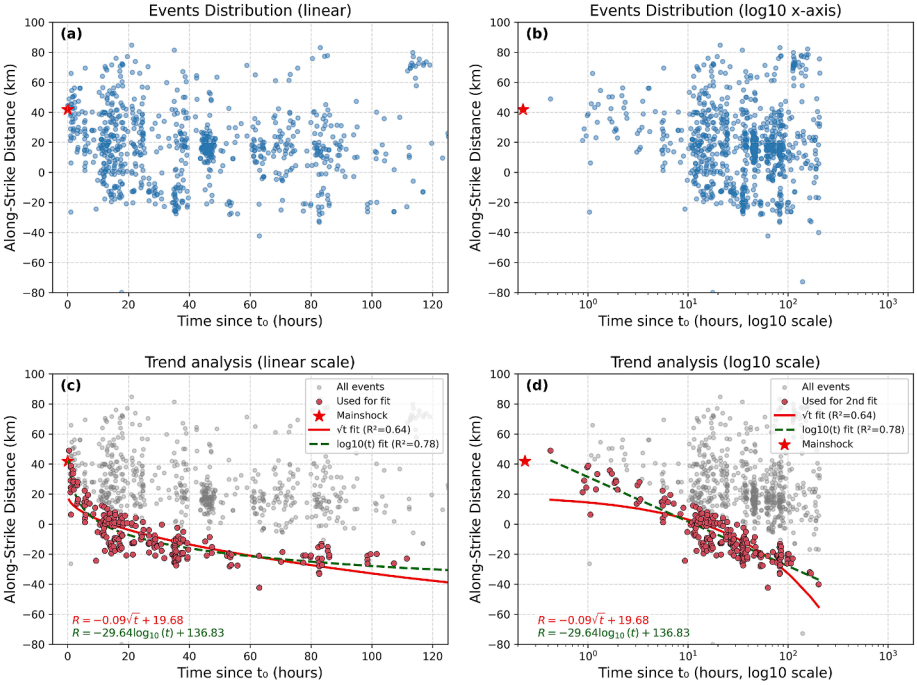

Fig. 6. Spatiotemporal evolution of seismicity along the fault. Panels (a) and (b) show the distribution of events from the template matching catalog with time since the reference origin (t_0) plotted on linear and logarithmic x-axes, respectively. Each dot represents an individual event, and the along-strike distance is measured relative to the mainshock location. Panels (c) and (d) present trend analyses for the same catalog, where the red points indicate the events used for fitting. Two empirical relationships are tested: the red solid line corresponds to a $\sqrt{t}$ fit ($R^2 = 0.67$), and the green dashed line corresponds to a $\log_{10}(t)$ fit ($R^2 = 0.80$).

R = −29.64 $\log_{10}$(t) + 136.83. Although both curves are close to each other in shape, the log10(t) function fits the aftershock expansion at the southern front better when compared to the sqrt(t) function. We also examine the spatial expansion for the M 7.0 event in 2024, the M 8.8 mainshock, and two M 7+ aftershocks (Fig. 5c). While a minor aftershock expansion is observed following the 2024 M_W 7.0 event, its spatial extent is limited. In addition, we observe a minor expansion of aftershocks in the NE direction following the 2025 M_W 8.8 mainshock. However, most of them occurred within the region marked by the dashed line (Fig. 5c), until the two $M_W > 7$ events in September 2025.

Next, we examine the continuous 5-min-sampling GNSS recording at PETT, which is accessible through the Nevada Geodetic Laboratory's network (Blewitt et al., 2009). We first rotate the two horizontal components from north-south and east-west to trench parallel and normal components using a strike of 217° from the M 8.8 mainshock (Fig. 7). The coseismic offset for the M_W 7.4 foreshock and the M_W 8.8 mainshock is obvious. In the foreshock window after the July 20, M_W 7.4 event, the trench normal component shows a steady seaward motion of a few centimeters that is well described by a simple logarithmic time fit, $d = 36 + 12 \log_{10}(1 + \frac{t}{1.71})$. On the other hand, the other two components do not show any obvious coseismic offset and postseismic deformation (Fig. 7b). Right after the July 29 mainshock, both trench normal and along strike components grow with a similar log-time form, $d = 466 + 39 \log_{10}(1 + \frac{t}{0.02})$ and $d = 344 + 33 \log_{10}(1 + \frac{t}{0.02})$ respectively, and reach several tens of centimeters by mid-August (Fig. 7a). The onset of trench-normal motion closely tracks the rise in cumulative local aftershocks.

6. Statistical analysis of foreshock and aftershock sequence

To further characterize the seismic sequence beside spatial patterns, we analyze the statistical aspects of the sequence using frequency-magnitude relationships, which include the mainshock, its strong foreshock sequence starting from July 20, 2025, and three significant aftershocks of the M_W 8.8 mainshock. Three analyzed aftershocks include a M_W 6.9 event that occurred 45 min after the mainshock, a M_W 6.8 that occurred on August 3, and a M_W 7.8 event that occurred on September 18. This is consistent with what is expected from Båth's law, which states that, on average, the magnitude difference between the mainshock and the largest aftershock is approximately 1.2 (Shcherbakov and Turcotte, 2004).

Because the local GSRAS catalog may exhibit variable magnitude completeness for offshore aftershocks due to station geometry and processing methods, we primarily use the global USGS catalog for the statistical analyses in this section. The USGS catalog provides more consistent magnitude estimates for large offshore earthquakes, which is important for robust identification of magnitude completeness. To model the sequence, we subdivide the seismic events according to three main time episodes. The first episode of the sequence constitutes events that occurred before the M_W 7.4 foreshock, starting from July 29, 2024, which can be treated as background seismicity. The second episode is characterized by the aftershocks of the M_W 7.4 event right before the occurrence of the M_W 8.8 mainshock, and the third episode comprises the main aftershock sequence.

The frequency-magnitude statistics of each episode of the sequence are plotted as an inset in Fig. 8. To model the observed frequency magnitude statistics, we use the Gutenberg-Richter (GR) relation (Gutenberg and Richter, 1944): $\log 10\,(N) = a - bM$. For the foreshocks of the M 7.4 event, we use all earthquakes above magnitude 4.5 and during the time interval starting on July 29, 2024 and ending right before the M_W 7.4 event. For the second time range, we consider all events between the M_W 7.4 event and the M_W 8.8 mainshock and above magnitude 4.5. Similarly, the aftershocks of the M_W 8.8 event are used above magnitude 4.5 up until November 4, 2025. The b-value of the M_W 8.8 aftershock sequence is calculated using only earthquakes within the same along-trench segment as the foreshock sequences, allowing a direct and consistent comparison. There is a notable change in b-value between foreshocks of the M_W 7.4 event and the subsequent aftershock sequence (Fig. 8).

In addition, we also model the rate of the occurrence of events during the evolution of the sequence. We fit the Epidemic Type Aftershock Sequence (ETAS) model to the sequence, including both foreshocks and aftershocks of the mainshock. The conditional intensity function $\lambda(t,H_t)$ of the ETAS model is defined as follows (Ogata, 1988; Harte, 2010):

$$\lambda(t|H_t) = \mu + K \sum_{i:t_i<t}^{n(t)} \frac{e^{\alpha(m_i - m_0)}}{\left(\frac{t-t_i}{C} + 1\right)^p} \quad (1)$$

where $\{\mu, K, c, p, \alpha\}$ are model parameters and μ specifies the average background rate of seismicity. The summation term represents the contribution to the total seismicity rate by $n(t)$ preceding events, which is performed over the occurrence of all past events above magnitude m_0 before time t. The parameters are estimated using the maximum likelihood method.

The result of the fitting of the ETAS model to the sequence for all events above magnitude 4.5 and during the target time interval $[T_s, T_e]$ between April 1, 2025 and November 4, 2025, is plotted in Fig. 9. We specify a time interval $[T_0, T_s]$ between 1 March and April 1, 2025, to properly calibrate the rate in the target time interval. The estimated

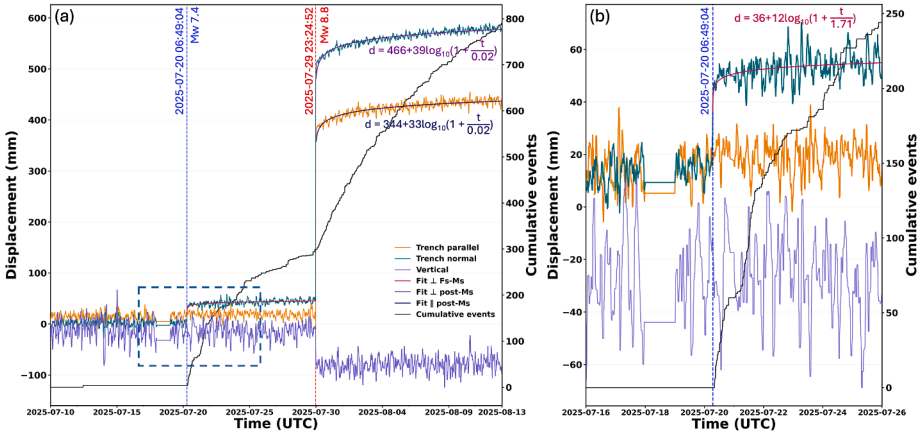

Fig. 7. (a) GNSS station PETT data in trench parallel, trench normal, and vertical starting from July 10, 2025 to August 13, 2025 with curve fit. (b) Zoom in on the blue box time range in (a) between July 16, 2025 and July 26, 2025.

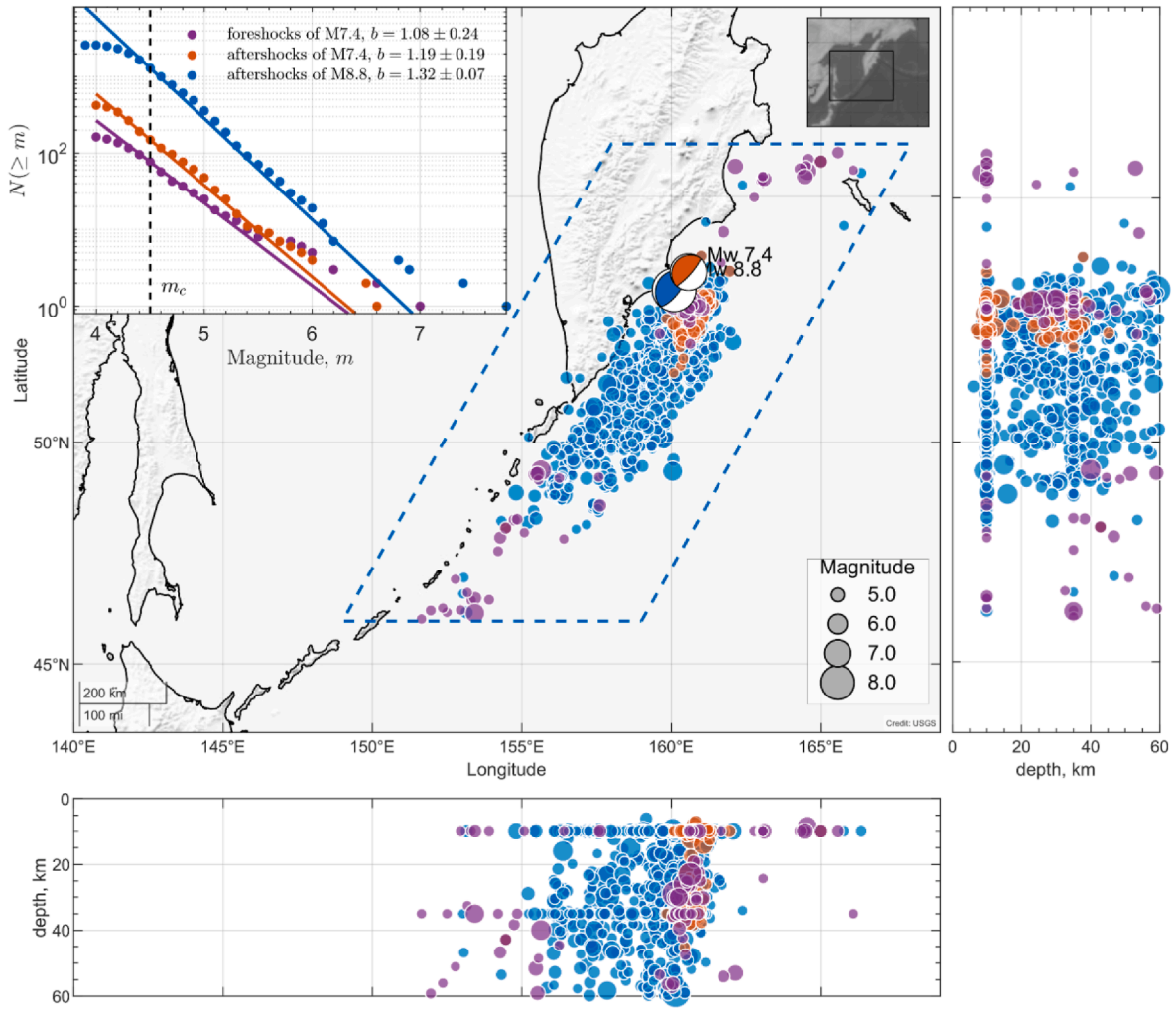

Fig. 8. Spatial distribution of events before and after the M_W 8.8 July 29, 2025, Kamchatka megathrust mainshock. Three episodes of the sequence, from USGS catalog, are illustrated: the foreshocks of the M_W 7.4 event - purple symbols, the aftershocks of the M_W 7.4 event - orange symbols, and the aftershocks of the M_W 8.8 mainshock - blue symbols. The inset shows the frequency magnitude distribution of each episode of the sequence. Two panels on the right and bottom provide the depth distribution of the corresponding events.

ETAS parameters are $[\mu, K, c, p, \alpha] = [0.08, 6.63, 0.022, 1.29, 1.30]$. To illustrate how the ETAS model describes the seismicity rate, we also plot the events and the cumulative numbers in Fig. 9. Overall, the model describes the sequence rate reasonably well with a slight underestimation of the rate in the August and September period of the aftershock sequence.

7. Waveform analysis of event productivity and statistical properties

The above analysis on the foreshock and aftershock behaviors is based on regular or enhanced earthquake catalogs, which are known to be incomplete immediately following the mainshock (Kagan, 2004), even after applying template-matching or machine-learning methods. Recently, several studies directly used amplitude distributions of the high-frequency envelope functions to quantify their statistical behaviors (Sawazaki, 2021; Shearer and Shakibay Senobari, 2025; Clements et al., 2025), including an attempt to discriminate between potential foreshocks and regular mainshock/aftershock sequences (Lippiello et al., 2025).

Here, we apply two methods to further quantify the statistical properties and event productivity following 5 $M_W > 7$ events (including the M_W 7.4 foreshock and the M_W 8.8 mainshock). In the first method, we use the square sum of the 2-16 Hz band-pass-filtered envelope function to compute the amplitude of completeness $A_c(t)$ before and after each target event (Clements et al., 2025). We use 5 days of continuous waveforms recorded at station IU.PET for the five events. A 5-day background curve before the 2025 M_W7.4 foreshock was also computed to illustrate the background noise and seismicity variability. Following Clements et al. (2025), we measure $A_c(t)$ as the 84% percentile of the logarithmic ground motion within a time window T. Here, we use a logarithmic time window length of 0.2, with a logarithmic sliding time window step of 0.01. Fig. 10a shows that $A_c(t)$ functions for all 5 target events decay logarithmically with time. However, their productivity levels are different. As expected, the curve for the M 8.8 mainshock has the highest productivity. The M 7.4 foreshock and the M 7.8 aftershock have the second-highest productivity, while the 2024 M 7.0 event and the M 7.4 aftershocks have the lowest aftershock productivity. Their $A_c(t)$ curves almost become flat near the end of the analysis time windows.

For comparison, we also compute the seismicity rates following these 5 M 7+ events, based on earthquakes listed in the USGS and USGS catalogs. We define the aftershock zones as the 2 times the source radius as determined by the USGS finite-fault solutions for the four M 7+ events. For the M_W 8.8 mainshock, we select its aftershock zone as the region immediately surrounding the mainshock rupture from the USGS

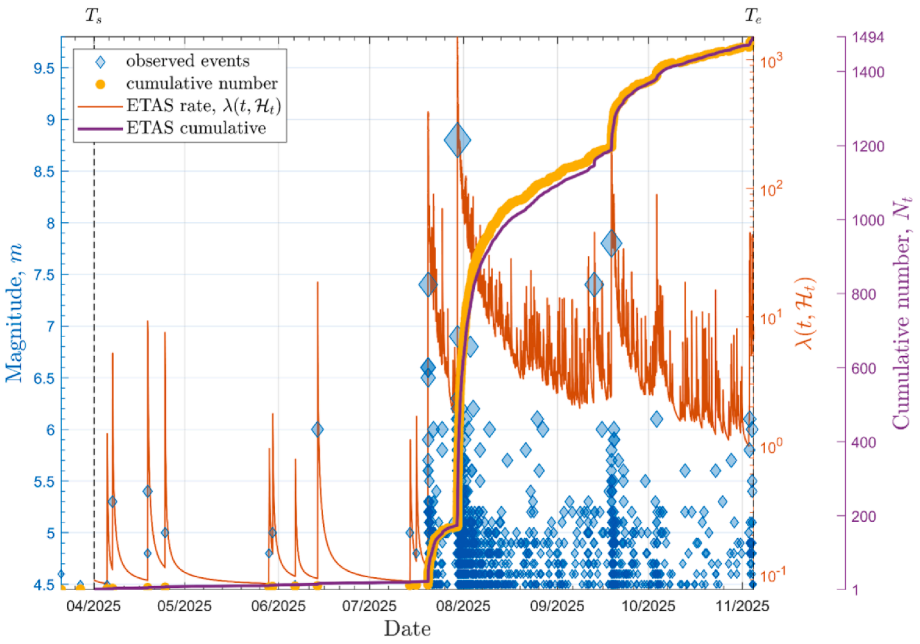

Fig. 9. The evolution of the 2025 Kamchatka earthquake sequence between April 1 and November 4, 2025. All events above magnitude 4.5 are shown as blue solid rhombus symbols. The fit of the ETAS model is given as a dark orange highly variable curve that gives the estimated conditional seismicity rate, $\lambda(t,H_t)$.

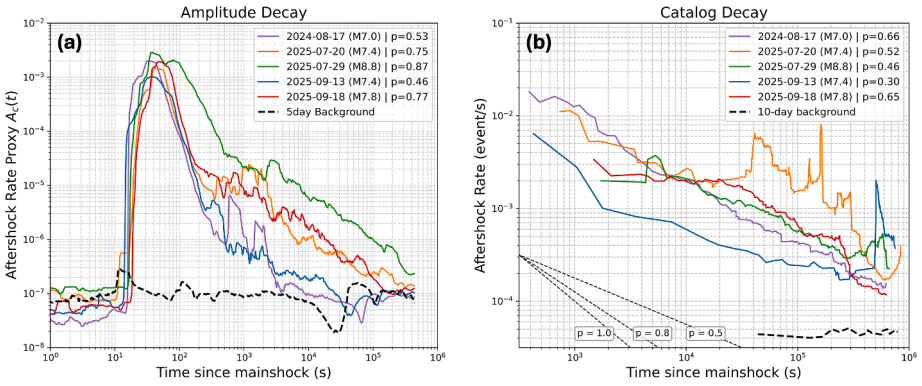

Fig. 10. (a) Amplitude of completeness Ac(t) curves for the 5 M 7+ sequences. The horizontal dashed lines mark the approximate 5-day background levels before the M_W 7.4 foreshock. (b) Aftershock rate decay for 5 M 7+ sequences with $M > 3$ based on GSRAS and USGS catalog. The horizontal dashed lines mark the approximate 10-day background levels before the M_W 7.4 foreshock. The dashed lines mark the Omori-law decay constant P value of 1, 0.8 and 0.5, respectively.

finite-fault solutions. We also use the sliding data window that begins with 4 aftershocks and ends with 200 aftershocks (Ziv, 2003). Fig. 10b shows that the aftershocks following the M 7.4 foreshock appear to have the highest aftershock productivity within the time scales of hours to days. The aftershock rate of the M_W 8.8 mainshock is in the middle, likely reflecting a significant lack of early aftershocks due to overlapping arrivals (Peng et al., 2007).

The second method attempts to quantify potential waveform differences and abnormal behaviors between the M 7.4 foreshock and the rest 4 M 7+ events (Lippiello et al., 2025). We calculate the Q value, which is another measure of the productivity of the sequence (Lippiello et al., 2025), as follows:

$$Q = \frac{n_{obs} K 10^{\delta\mu}}{10^{\beta\mu M}} \tag{2}$$

where n_{obs} is determined following the method of Peng et al. (2007) for $\mu(t)$ within the first 45 min after the mainshock, counted manually. The coefficient K is introduced as described in Lippiello et al. (2019). Here we use a value of 100. Both $\delta\mu$ and μ_M are obtained from the band-pass-filtered envelopes, using a time window of 400 s before and 45 min after the original time, with a smoothing parameter of 5. The parameter β is approximately equal to the b-value of the Gutenberg–Richter law. We consider cases with β = 1.0, 0.8, 0.7, and 0.4. Lippiello et al. (2025) found a possible threshold of Q = 0.18 for selected $M > 6$ events around the world, above which the target event could be considered as a possible foreshock, defined as an earthquake that is followed within 10 days by a larger event within 50 km.

Fig. 11 shows the 2-16 Hz band-pass-filtered envelope functions and the corresponding Q values. The case with $\beta = 1$ corresponds to Q′, the Q value without multiplication by n_{obs} in Equation (2), representing the minimum possible value. Specifically, for the events on August 17, 2024, July 20, 2025, and September 13, 2025, the corresponding Q' values are 2.0, 0.8, and 1.6, respectively. Regardless of the choice of n_{obs}, these values remain greater than 0.18. For the M 7.8 aftershock on September 18, 2025, the number of observed aftershocks (n_{obs}) is significantly larger than 8, also leading to Q > 0.18. The only exception is the M 8.8 mainshock, whose Q value is relatively small and inconsistent with the observed seismicity. The Q value associated with each β value can be found in Table S1 in the Supplementary Material.

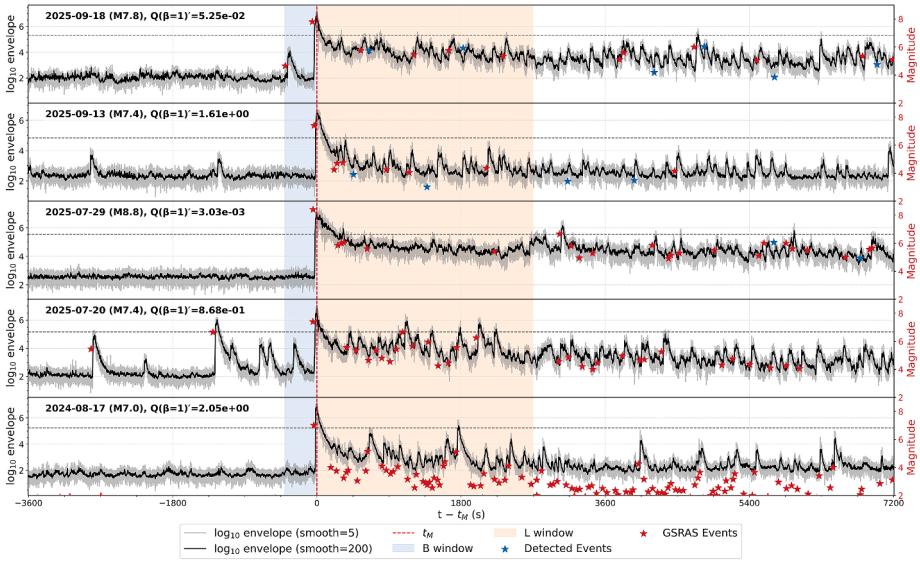

Fig. 11. Examples of envelope fitting and Q value calculation for four mainshocks with $M > 7$. The black curves show the smoothed logarithmic envelopes (smooth sample = 5), while the vertical lines indicate the fitting windows for μ_M, μ_B, and μ_L. The calculated Q values are reported for different β parameters (β = 1.0, 0.8, 0.7, 0.4). These results illustrate that the obtained Q values strongly depend on the assumed β, but even the minimum values (β = 1) are significantly larger than the threshold of 0.18 for most events, suggesting that these earthquakes can be considered potential foreshocks.

To further test the general applicability of this method, we extend the calculation to all events with magnitudes larger than 6.0 occurring between August 17, 2024 and September 23, 2025 (Fig. 12). In this broader analysis, we set $n_{obs} = 1$ and K = 1, thereby obtaining the minimum possible Q values. The Q values fluctuate over time and do not show any obvious patterns. For example, the events on August 30, 2024 (M 6.1) and September 30, 2024 (M 6.2) were not followed by larger events within 10 days, yet their minimum Q values still exceeded 0.18 (Fig. 12).

8. Discussion and conclusions

In this study we present detailed analysis of the July 29, 2025 M_W 8.8 Kamchatka earthquake sequence using a combination of multiple approaches and techniques, including single-station template matching with the existing local catalogs, seismicity statistical analysis, teleseismic back-projection, and geodetic constraints. We observe the spatiotemporal evolution from foreshock through early aftershocks of the M_W 8.8 event, with the emphasis on the possibility of afterslip-driven seismicity expansion between the largest foreshock event and the mainshock. We also find a relatively high aftershock productivity of the M 7.4 foreshock when compared with other M 7+ events in this region.

Here we compare our results of the mainshock rupture properties with other recent studies in this region. The spatial relationships among the 2025 M_W 8.8 rupture, major historical earthquake rupture zones, and regional geological features are illustrated in Fig. 13. Our back-projection of teleseismic P waves from three continental arrays all show a predominant southwest rupture for 500 km over about 220 s, with an average rupture speed near 2.3 km/s. This is largely consistent with other back-projection results (e.g., Xu et al., 2025; Yin et al., 2026; Liu et al., 2026; Shibata et al., 2025; Tarumi and Yoshizawa, 2025). Multiple bursts of high-frequency energy are seen with short pauses, consistent with failure of multiple patches on the plate interface obtained from finite-fault modeling (Yagi et al., 2025; Xu et al., 2025; Yin et al., 2026; Liu et al., 2026). Another robust feature from our and other studies is that the mainshock slip appears to stop near Cape Shipunskiy.

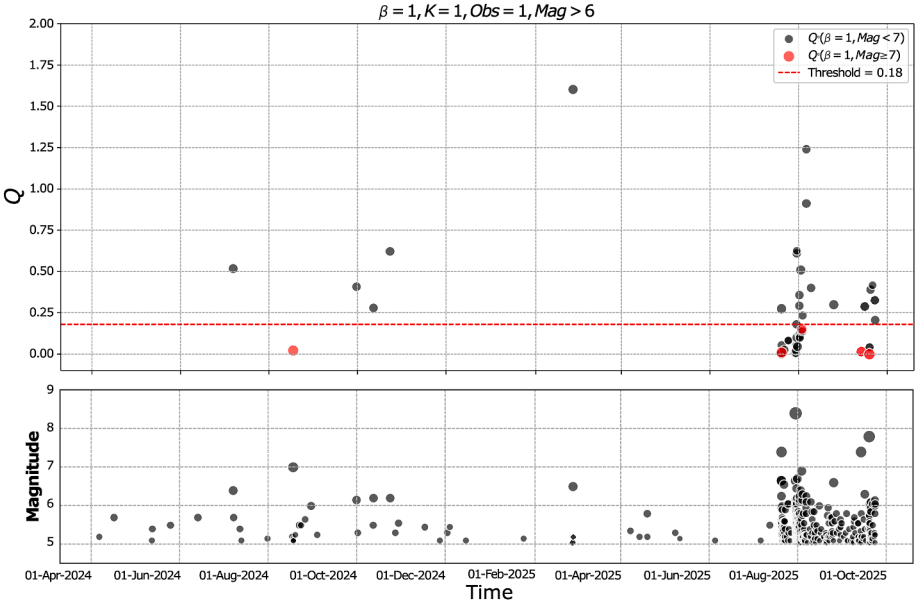

Fig. 12. Temporal distribution of Q′ values for earthquakes with $M > 6$ between July 2024 and September 2025, calculated with β = 1, K = 1, and $n_{obs} = 1$. Black circles represent events with $6.0 < M < 7.0$, and red circles represent events with $M > 7.0$. The dashed red line marks the threshold of Q = 0.18.

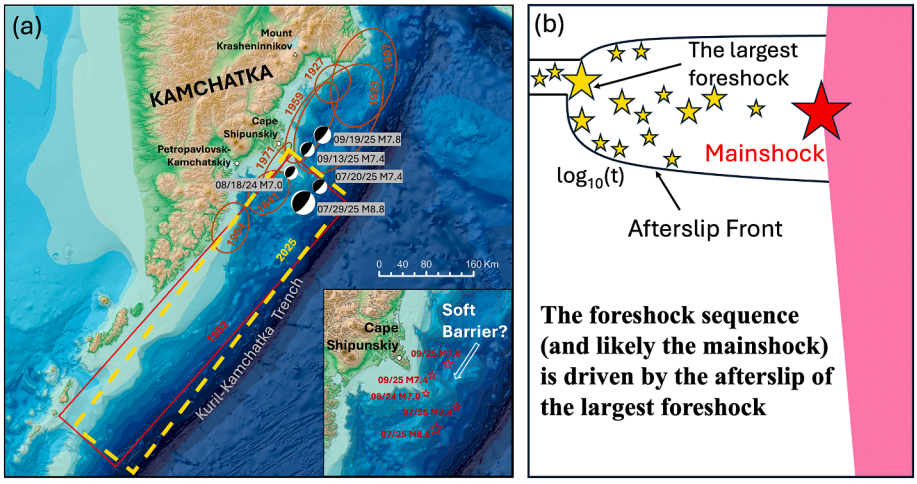

Fig. 13. (a) Kamchatka Peninsula map with rupture zones of significant historical earthquakes (orange) with the focus estimated rupture zones of the 1952 event (red) and the 2025 event (dashed yellow). The inset shows zoomed in of Cape Shipuskiy region with 5 mentioned focusing events. (b) The schematic diagram of the proposed foreshock model for the sequence of the M_W 7.4 foreshock and the M_W 8.8 mainshock.

The 1952 M_W 8.8-9.0 Kamchatka earthquake ruptures shared some similarity to the 2025 event, although the 1952 mainshock slip appears to complement with the 2025 rupture (Mikhailov et al., 2025; Yagi et al., 2025), and its aftershocks showed possible slip northeast of Cape Shipunskiy (MacInnes et al., 2010; Yagi et al., 2025).

Fig. 13a illustrates the 2025 rupture in a broader historical context, highlighting the overlapped seismic areas and initiation of large ruptures near Cape Shipunskiy. In addition to the 1952 and 2025 mainshocks, other events, such as the 1923 *M* 8.4, 1959 *M* 8.3, and 1971 *M* 7.6 events (Chebrov, 2025), as well as the 2024 *M* 7.0 (Chebrov et al., 2025) and 09/13/2025 *M* 7.4 and 09/19/2025 *M* 7.8 earthquakes, all occurred on either side of Cape Shipunskiy. We argue that the segment near Cape Shipunskiy acts as a "soft barrier" (Wang et al., 2025), where the segment may occasionally stop earthquake rupture from propagating through, but in other cases, it may participate in the rupture or initiate ruptures. Such a soft barrier can exist in the down-dip directions, for example in the serpentinized mantle wedge of the Chile subduction zone (Wang et al., 2020, 2025), or in the along-strike directions, such as the possible "soft barrier" at the tip of the Kii Peninsula in the Southwest Japan subduction zone, which separated the 1944 Tonankai M_W 8.1 and the 1946 Nankai M_W 8.4 earthquakes into distinct rupture zones (Ando, 1975; Kodaira et al., 2006). However, in previous earthquake cycles, these adjacent rupture zones either ruptured in one single event (e.g., the 1707 M_W 8.7 Hōei earthquake), or two events in the 1854 Ansei great earthquake sequences that were only 31 h apart. Bassett and Watts (2015a, 2015b) found negative free-air gravity anomalies in the large earthquake rupture zones surrounding Cape Shipunskiy where an extended continental shelf can be seen from the sea floor bathymetry (Fig. 13a). In continental thrust faults, recent studies also revealed potential contributions of the hanging wall topography and excess weight in controlling the segmentation of large thrust earthquakes such as the 2008 M_W7.9 Wenchuan earthquake (Styron and Hetland, 2015; Tan et al., 2018). These studies highlight the need to better understand the interplay among the geometry and material properties of overriding (and incoming) plates, the frictional properties, and diverse fault-slip behaviors along the plate interface.

In this study, we find a clear along-strike expansion of seismicity following the largest foreshock of *M* 7.4 that occurred 10 days before the *M* 8.8 mainshock. The expansion fits the log10(t) function slightly better than the $\sqrt{t}$ function, which is more consistent with, but not unique to, an afterslip-driven mechanism. At the same time, we also find a similar log10(t) decay in the trench normal displacement following the *M* 7.4 foreshock, consistent with the log10(t)-type aftershock expansion. Hence, we propose yet another foreshock model (Fig. 13b) where the largest foreshock and its subsequent afterslip trigger the mainshock nucleation. Note that this model is not new, because similar models, such as the rate-dependent cascade-up model (McLaskey, 2019), have been proposed before. In addition, Noda et al. (2013) have shown that precursory earthquakes (i.e., foreshocks) can be followed by larger afterslip than non-precursory ones. In the migratory slow-slip model (Wang et al., 2024), a migrating slow slip occurs before the largest foreshock. Here, the largest foreshock occurs first, triggers afterslip (likely larger than expected), and then the mainshock. We note that this model differ slightly with a recently proposed model where a transient slow-slip event occurred a few hours later and then followed by a mainshock (Yue et al., 2026). It is possible that slow slip occurred before the *M* 7.4 foreshock, but besides several moderate-size events (*M* 5-6) occurring right before (Fig. 11), we do not have any additional evidence to argue for the existence of precursory slow slip before the *M* 7.4 foreshock and the *M* 8.8 mainshock. In addition, we find that the *M* 7.4 foreshock was indeed followed by an energetic aftershock sequence with more expansion and higher productivity than the other three *M* 7+ events in the same region. However, the 2024 *M* 7.0 event was smaller and deeper, whereas the other two events (*M* 7.4 and *M* 7.8) were aftershocks of the *M* 8.8 mainshock, and their source properties and triggering mechanism might also be different. While a connection between the 2024 *M* 7.0 event and the 2025 *M* 7.4 foreshock cannot be ruled out, the intervening seismic activity does not show a clear, systematic evolution linking the two events. A systematic comparison of similar-sized events in other regions is needed to better establish the uniqueness of this foreshock sequence.

Migrating foreshocks preceding great subduction earthquakes have been documented before the 2011 *M* 9.1 Tohoku-Oki and 2014 *M* 8.1 Iquique earthquakes (Kato et al., 2012; Kato and Nakagawa, 2014; Ruiz et al., 2014). In both cases, slow slip was invoked as the driving mechanism for the foreshock migration and mainshock nucleation, and geodetic instruments also recorded both long and short-term slow slip signals (Ito et al., 2013; Ruiz et al., 2014), although the 2-h-long precursory slip before the 2011 Tohoku-Oki and other large earthquakes is still in debate (Bletery and Nocquet, 2023, 2025; Hirose et al., 2024). Recent single-station observations of the 2025 M_W 8.8 Kamchatka sequence also documented foreshock migration toward the mainshock hypocenter, providing additional evidence for aseismic slip consistent with our observations (Zhang et al., 2025). However, we expect that moderate to large foreshocks are followed by its own aftershocks that expand with time, which are likely triggered by afterslip that propagates outwards following the log10(t) expansion (Kato, 2007; Peng and Zhao, 2009), as well as decaying with time similar to the Omori's law

aftershock decay (Perfettini and Avouac, 2004, 2007; Hsu et al., 2006; Utsu et al., 1995). Other stress-triggering mechanisms can also trigger aftershocks (Freed, 2005). Hence, the presence of the expanding aftershocks and afterslip following a moderate-to-large earthquake is not enough to guarantee that it will be followed by a larger event. However, one can potentially examine whether the expanding speed and region of aftershocks following the M 7.4 foreshock (and other foreshocks such as the 2011 M 7.3 foreshock before the M 9.1 Tohoku-Oki earthquake) is abnormal or not.

In recent years, multiple methods have been used to study whether a large event is a mainshock itself or a foreshock to a larger event by investigating the sequence statistical behavior, which includes tracking the changes in b-value, amplitude of completeness, and calculating the immediate envelope-based productivity Q (Schorlemmer et al., 2005; Nanjo et al., 2012; Gulia and Wiemer, 2019; Lippiello et al., 2019, 2025). In this Kamchatka sequence, an increase in b-value is observed from the background before the M_W 7.4 foreshock window to the aftershocks of the M_W 8.8 mainshock (Fig. 8). This is different with the interpretation of a drop in b-value drop during a potential foreshock sequence (Gulia and Wiemer, 2019). The largest change in the b-value occurred before and after the mainshock (Fig. 8). However, a change in b-value around the mainshock is somewhat expected, which can be caused by a combination of factors such as changes in the magnitude of completeness (Mc) or changes in the differential stress levels following the mainshock (Tormann et al., 2015; Gulia and Wiemer, 2019; van der Elst, 2021; Ito and Kaneko, 2023). We do not attempt to compute a more fine-scale changes in b-value in this study, mainly because the catalog we have obtained (a combined local GSRAS catalog and a single-station template-matching catalog) still misses many aftershocks, especially immediately following the M 7.4 foreshock and the M 8.8 mainshock (Fig. 5). A comparison between the 2024 M 7.0 event and the 2025 M 7.4 foreshock would also be valuable for assessing their relative triggering potential, but such an analysis is beyond the resolution of the current dataset.

Our amplitude-decay analysis result shows consistent Omori's law-type decay pattern but highlights different productivity rankings with the M 8.8 sequence dominating in the amplitude proxy because many early aftershocks overlap and elevate the envelope level (Fig. 10). The M 7.4 foreshock appears to be the second most productive (after the M8.8 mainshock), with its aftershock levels matching that from the M 7.8 aftershock. High foreshock productivity is often followed by enhanced short-term aftershock productivity, consistent with a cascade-type response of the system (Marsan et al., 2014). A transient aseismic slip can further amplify this pattern, as documented for the 2017 Valparaiso sequence (Moutote et al., 2023). This observation is consistent with the finding by Stein et al. (2025), indicating that more productive moderate-size earthquake sequences may have higher potential to become a foreshock sequence (Wetzler et al., 2023). In the Q calculation, our results show a consistency with a strong early productivity sequence, where events exceed the $Q > 0.18$ threshold with reasonable choices of β and window (Peng et al., 2007; Lippiello et al., 2019, 2025). However, this method shows several false positives when extending the same calculation to many M 6 to M 7 events in this sequence (Fig. 12). We argue that the Q analysis (Lippiello et al., 2025) is sensitive to β, the early time count, and completeness in the first few hours, which cannot be easily applied in a real-time setting to discriminate between real foreshocks from normal earthquake sequences.

Our preliminary results are affected by the limitation of the data availability and station coverage. Continuous waveforms were available from one nearby broadband station only (IU.PET), and only one GNSS station (PETT) had accessible 5-min displacement recording. The matched-filter detections are limited by the template event from the obtained catalog, in which the absolute locations of detected events remain uncertain due to the assignment of template locations. In addition, the number of new detected events is not significant compared to those with more station coverage (Peng and Zhao, 2009; Neves et al., 2024), as it is a challenge to achieve all the hidden events from one station's waveforms. Although the GNSS record has a high sampling rate (5-min per sample), it remains insufficient for resolving any immediate change in displacement within short time window right before the M_W 8.8 mainshock, which is essential to observe any precursory signals large earthquake (Bletery and Nocquet, 2023). Recent work using submarine optical fiber measurement detected precursory polarization changes prior to the mainshock, indicating the subtle strain perturbations associated with nucleation process can be observed using high-sensitivity sensing system (Mecozzi et al., 2025). In addition, to further improve this study, a more complete continuous seismic and geodetic data coverage is required to build a high-resolution catalog. Despite the current data limitations, our results demonstrate the value of analyzing seismic activities, back-projection, and geodetic observations to identify foreshock behavior and rupture segmentation. Combining with multi-station geodetic recordings and other geophysical observations (Shelly, 2024), the physical mechanisms of the foreshock generation and mainshock nucleation can be better refined (Peng and Lei, 2025). Accurately identifying those sequences with abnormal behaviors can help to improve our ability to forecast short-term low-probability events (Hardebeck et al., 2024), which is essential for operational earthquake forecasting (Jordan et al., 2011; Goltz, 2025).

Taken together, the observations support a segmented rupture on the Kuril-Kamchatka interface and a plausible afterslip between the M_W 7.4 foreshock and the M_W 8.8 mainshock within the limits of the available data. Back projection indicates a predominant southwestward rupture with several sub-events during the mainshock, while the geodetic record provides constraints through the coseismic deformation, and a deficit of seismic activity to the northeast of the mainshock hypocenter inferred from historical earthquakes and additional geophysical observations. The Q values and the change in b-value provide a summary of the strong early productivity of the largest events; however, their utility is limited by data completeness and parameter choices, and therefore they are used here as descriptive indicators rather than predictors.

In summary, our results demonstrate that integrating back-projection, enhanced seismic catalog, and limited geodetic observations can still resolve important features of foreshock activity, rupture segmentation, and early postseismic behavior for great subduction earthquakes. This integrated framework can be used to provide rapid assessment for seismic and tsunami hazard along the Kamchatka, highlighting how foreshock activity can influence the spatial extent and cascading potential of great subduction earthquakes. Future studies incorporating both onshore and offshore seismic observations, improved velocity models, and multi-station matched-filter detection will further refine earthquake locations and better illustrate seismic behaviors before and after great subduction earthquakes.

CRediT authorship contribution statement

Phuc Mach: Writing – review & editing, Writing – original draft, Visualization, Methodology, Investigation, Formal analysis, Data curation, Conceptualization. **Xu Si:** Writing – review & editing, Visualization, Software, Methodology, Investigation, Formal analysis. **Dun Wang:** Writing – review & editing, Visualization, Methodology, Investigation, Formal analysis. **Robert Shcherbakov:** Writing – review & editing, Visualization, Methodology, Investigation, Formal analysis. **Ping He:** Writing – review & editing, Visualization, Methodology, Investigation, Formal analysis. **Tuncay Taymaz:** Writing – review & editing, Supervision, Resources, Data curation. **Chang Ding:** Writing – review & editing, Visualization, Formal analysis. **Zhigang Peng:** Writing – review & editing, Validation, Supervision, Investigation, Formal analysis, Data curation, Conceptualization.

Declaration of competing interest

The authors declare the following financial interests (e.g., any funding for the research project)/personal relationships (e.g., the author is an employee of a profitable company) which may be considered as potential competing interests: Zhigang Peng is the Deputy Editor-in-Chief for Earthquake Research Advances and was not involved in the editorial review or the decision to publish the article. Dun Wang and Tuncay Taymaz are the Associate Editors for Earthquake Research Advances and were not involved in the editorial review or the decision to publish the article.

Acknowledgements

We acknowledge Prof. Aleksey A. Emanov's enthusiastic approach to accessing the current seismicity catalogs, and Evgeny A. Matveenko and Dr. Danila Chebrov of the Kamchatka Branch of Geophysical Survey, RAS, Petropavlovsk-Kamchatsky, Russia, for providing permission to the local earthquake catalog. The data used in the work were obtained with large-scale research facilities "Seismic infrasound array for monitoring Arctic cryolitozone and continuous seismic monitoring of the Russian Federation, neighbouring territories and the world" (https://ckp-rf.ru/usu/507436/, http://www.gsras.ru/unu/). The manuscript benefits from comments by Professors Roland Burgmann, Yangfan Deng, and Jing Wu. P.M., X.S., C.D. and Z.P. are partially supported by U.S. National Science Foundation grant RISE-2425889. Tuncay Taymaz thanks Istanbul Technical University (ITU-BAP) and Disaster Management Institute (ITU-AYE) for allocating research funds and environment during the recent hectic and chaotic years.

Appendix A. Supplementary data

Supplementary data to this article can be found online at https://doi.org/10.1016/j.eqrea.2026.100457.

References

Ammon, C., Kanamori, H., Lay, T., 2008. A great earthquake doublet and seismic stress transfer cycle in the central Kuril Islands. Nature 451, 561–565. https://doi.org/10.1038/nature06521.

Ando, M., 1975. Source mechanisms and tectonic significance of historical earthquakes along the Nankai Trough, Japan. Tectonophysics 27 (2), 119–140. https://doi.org/10.1016/0040-1951(75)90102-X.

Bassett, D., Watts, A.B., 2015a. Gravity anomalies, crustal structure, and seismicity at subduction zones: 1. Seafloor roughness and subducting relief. G-cubed 16, 1508–1540. https://doi.org/10.1002/2014GC005684.

Bassett, D., Watts, A.B., 2015b. Gravity anomalies, crustal structure, and seismicity at subduction zones: 2. Interrelationships between fore-arc structure and seismogenic behavior. G-cubed 16, 1541–1576. https://doi.org/10.1002/2014GC005685.

Beroza, G.C., Segou, M., Ellsworth, W.L., 2021. Machine learning and earthquake forecasting—next steps. Nat. Commun. 12, 4761. https://doi.org/10.1038/s41467-021-24952-6.

Bilek, S.L., Lay, T., 2018. Subduction zone megathrust earthquakes. Geosphere 14 (4), 1468–1500. https://doi.org/10.1130/GES01608.1.

Bletery, Q., Nocquet, J.M., 2023. The precursory phase of large earthquakes. Science 381 (6655), 297–301. https://doi.org/10.1126/science.adg2565.

Bletery, Q., Nocquet, J.-M., 2025. Do large earthquakes start with a precursory phase of slow slip? Seismica 3 (2). https://doi.org/10.26443/seismica.v3i2.1383.

Blewitt, G., Hammond, W.C., Kreemer, C., et al., 2009. GPS for real-time earthquake source determination and tsunami warning systems. J. Geod. 83 (3-4), 335–343. https://doi.org/10.1007/s00190-008-0262-5.

Bradley, K., Hubbard, J., 2024. M7.1 strikes offshore Kamchatka – in an area that nucleated a M9 in 1952. Earthquake insights. https://doi.org/10.62481/33403660.

Bradley, K., Hubbard, J., 2025a. A first look at the Mw8.8 Kamchatka earthquake. Earthquake Insights. https://doi.org/10.62481/f8aeb017.

Bradley, K., Hubbard, J., 2025b. M 7.8 strikes offshore Kamchatka. Earthquake insights. https://doi.org/10.62481/98dfff39.

Chebrov, D., 2025. Kamchatka mega-earthquake of July 29, 2025 (Mw = 8.8) (In Russian). Bull. Kamchatka Regional Association Earth Sci. (KRAUNTS), 67 (3). https://doi.org/10.31431/1816-5524-2025-3-67-113-117.

Chebrov, D.V., Matveenko, E.A., Abubakirov, I.R., Droznina, S.Y., Lander, A.V., Mityushkina, S.V., Pavlov, V.M., Raevskaya, A.A., Saltykov, V.A., Senyukov, S.L., Titkov, N.N., 2025. The Mw 7.0 Shipunsky Earthquake of August 17, 2024 off the East Coast of Kamchatka. J. Volcanol. Seismol. 19 (3), 271–280. https://doi.org/10.1134/S0742046325700101.

Chebrov, V.N., Droznin, D.V., Kugaenko, Y.A., Levina, V.I., Senyukov, S.L., Sergeev, V.A., Shevchenko, Y.V., Yashchuk, V.V., 2013. The system of detailed seismological observations in Kamchatka in 2011. J. Volcanol. Seismol. 7 (1), 16–36. https://doi.org/10.1134/S0742046313010028.

Chebrova, A.Y., Chemarev, A.S., Matveenko, E.A., Chebrov, D.V., 2020. Seismological data information system in Kamchatka branch of GS RAS: organization principles, main elements and key functions (In Russian). Geophys. Res. 21 (3), 66–91. https://doi.org/10.21455/gr2020.3-5.

Clements, T., Cochran, E.S., Minson, S.E., van der Elst, N.J., Yoon, C.E., Baltay, A., Page, M.T., 2025. Mechanics and statistics of postseismic shaking. Geophys. Res. Lett. 52, e2025GL116673. https://doi.org/10.1029/2025GL116673.

DeMets, C., Gordon, R.G., Argus, D.F., 2010. Geologically current plate motions. Geophys. J. Int. 181 (1), 1–80. https://doi.org/10.1111/j.1365-246X.2009.04491.x.

Eggert, S., Walter, T.R., 2009. Volcanic activity before and after large tectonic earthquakes: observations and statistical significance. Tectonophysics 471 (1–2), 14–26. https://doi.org/10.1016/j.tecto.2008.10.003.

Freed, A.M., 2005. Earthquake triggering by static, dynamic, and postseismic stress transfer. Annu. Rev. Earth Planet Sci. 33 (1), 335–367. https://doi.org/10.1146/annurev.earth.33.092203.122505.

Gibbons, S.J., Ringdal, F., 2006. The detection of low-magnitude seismic events using array-based waveform correlation. Geophys. J. Int. 165 (1), 149–166. https://doi.org/10.1111/j.1365-246X.2006.02865.x.

Global Volcanism Program (GVP), 2025. Kamchatka Volcano Activity Reports. Smithsonian Institution. https://volcano.si.edu/ (accessed 2 October 2025).

Goltz, J.D., 2025. Are Short-Term Low-Probability earthquake forecasts useful? An emergency management perspective. Seismol Res. Lett. https://doi.org/10.1785/0220250273.

Gulia, L., Wiemer, S., 2019. Real-time discrimination of earthquake foreshocks and aftershocks. Nature 574, 193–199. https://doi.org/10.1038/s41586-019-1606-4.

Gutenberg, B., Richter, C.F., 1944. Frequency of earthquakes in California. Bull. Seismol. Soc. Am. https://doi.org/10.1785/BSSA0340040185.

Hardebeck, J.L., Llenos, A.L., Michael, A.J., Page, M.T., Schneider, M., van der Elst, N.J., 2024. Aftershock forecasting. Annu. Rev. Earth Planet Sci. 52, 61–84. https://doi.org/10.1146/annurev-earth-040522-102129.

Harte, D., 2010. PtProcess: an R package for modelling marked point processes indexed by time. J. Stat. Software 35 (8), 1–32. https://doi.org/10.18637/jss.v035.i08.

Hayes, G.P., Moore, G.L., Portner, D.E., Hearne, M., Flamme, H., Furtney, M., Smoczyk, G.M., 2018. Slab 2, a comprehensive subduction zone geometry model. Science 362 (6410), 58–61. https://doi.org/10.1126/science.aat4723.

Himematsu, Y., Munekane, H., 2025. Shallow segment rupture associated with the 2025 Kamchatka earthquake inferred from ALOS-2/PALSAR-2 InSAR. Earth Planets Space. https://doi.org/10.21203/rs.3.rs-8111287/v1 in review.

Hirose, H., Kato, A., Kimura, T., 2024. Did short-term preseismic crustal deformation precede the 2011 great Tohoku-oki earthquake? An examination of stacked tilt records. Geophys. Res. Lett. 51, e2024GL109384. https://doi.org/10.1029/2024GL109384.

Hsu, Y.-J., Simons, M., Avouac, J.-P., Galetzka, J., Sieh, K., Chlieh, M., Natawidjaja, D., Prawirodirdjo, L., Bock, Y., 2006. Frictional afterslip following the 2005 Nias–Simeulue earthquake, Sumatra. Science 312 (5782), 1921–1926. https://doi.org/10.1126/science.1126960.

Hubbard, J., Bradley, K., 2025a. M7.4 earthquake strikes the Kamchatka Peninsula. Earthquake Insights. https://doi.org/10.62481/a8be96de.

Hubbard, J., Bradley, K., 2025b. Updates on the Kamchatka earthquake. Earthquake insights. https://doi.org/10.62481/69d32d61.

Ito, R., Kaneko, Y., 2023. Physical mechanism for a temporal decrease of the Gutenberg–Richter b-value prior to a large earthquake. J. Geophys. Res. Solid Earth 128, e2023JB027413. https://doi.org/10.1029/2023JB027413.

Ishijima, K., Watada, S., 2026. The slip distribution of the 2025 Kamchatka earthquake estimated from dispersive tsunami images observed by SWOT satellite. ESS Open Archive. https://doi.org/10.22541/essoar.177032873.37227439/v1.

Ito, Y., Hino, R., Kido, M., Fujimoto, H., Osada, Y., Inazu, D., Ohta, Y., Iinuma, T., Ohzono, M., Miura, S., Mishina, M., 2013. Episodic slow slip events in the Japan subduction zone before the 2011 Tohoku-Oki earthquake. Tectonophysics 600, 14–26. https://doi.org/10.1016/j.tecto.2012.08.022.

Johnson, J., Satake, K., 1999. Asperity distribution of the 1952 great Kamchatka earthquake and its relation to future earthquake potential in Kamchatka. Pure Appl. Geophys. 154, 541–553. https://doi.org/10.1007/s000240050243.

Jordan, T.H., Chen, Y.T., Gasparini, P., Madariaga, R., Main, I., Marzocchi, W., Papadopoulos, G., Sobolev, G., Yamaoka, K., Zschau, J., 2011. Operational earthquake forecasting: state of knowledge and guidelines for utilization. Ann. Geophys. 54 (4), 315–391. https://doi.org/10.4401/ag-5350.

Kagan, Y.Y., 2004. Short-term properties of earthquake catalogs and models of earthquake source. Bull. Seismol. Soc. Am. 94 (4), 1207–1228. https://doi.org/10.1785/012003098.

Kato, N., 2007. Expansion of aftershock areas caused by propagating post-seismic sliding. Geophys. J. Int. 168 (2), 797–808. https://doi.org/10.1111/j.1365-246X.2006.03255.x.

Kato, A., Nakagawa, S., 2014. Multiple slow-slip events during a foreshock sequence of the 2014 Iquique, Chile Mw 8.1 earthquake. Geophys. Res. Lett. 41, 5420–5427. https://doi.org/10.1002/2014GL061138.

Kato, A., Obara, K., Igarashi, T., Tsuruoka, H., Nakagawa, S., Hirata, N., 2012. Propagation of slow slip leading up to the 2011 Mw 9.0 Tohoku-Oki earthquake. Science 335 (6069), 705–708. https://doi.org/10.1126/science.1215141.

Kiser, E., Ishii, M., 2017. Back-projection imaging of earthquakes. Annu. Rev. Earth Planet Sci. 45, 271–299. https://doi.org/10.1146/annurev-earth-063016-015801.

Kodaira, S., Hori, T., Ito, A., Miura, S., Fujie, G., Park, J.-O., Baba, T., Sakaguchi, H., Kaneda, Y., 2006. A cause of rupture segmentation and synchronization in the Nankai trough revealed by seismic imaging and numerical simulation. J. Geophys. Res. 111, B09301. https://doi.org/10.1029/2005JB004030.

Kopylova, G.N., Serafimova, Y.K., Kasimova, V.A., 2025. The occurrence of precursors before large (MW $\geq$ 6.6) Kamchatka earthquakes. J. Volcanol. Seismol. 19, 172–195. https://doi.org/10.1134/S0742046325700034.

Kozhurin, A., Zelenin, E., 2017. An extending island arc: the case of Kamchatka. Tectonophysics 706–707, 91–102. https://doi.org/10.1016/j.tecto.2017.04.001.

Lippiello, E., Petrillo, G., Godano, C., Tramelli, A., Papadimitriou, E., Karakostas, V., 2019. Forecasting of the first-hour aftershocks by means of the perceived magnitude. Nat. Commun. 10, 2953. https://doi.org/10.1038/s41467-019-10763-3.

Lei, X., Wang, Z., Ma, S., He, C., 2024. Step-over of strike-slip faults and overpressure fluid favor occurrence of foreshocks: Insights from the 1975 Haicheng fore-main-aftershock sequence, China. Earthq. Res. Adv. 4 (1), 100237. https://doi.org/10.1016/j.eqrea.2023.100237.

Lippiello, E., Petrillo, G., Godano, C., Dal Zilio, L., 2025. Toward recognizing the waveform of foreshocks. Geophys. Res. Lett. 52, e2025GL115466. https://doi.org/10.1029/2025GL115466.

Liu, C., Bai, Y., Lay, T., He, P., Wen, Y., Xiong, X., Taymaz, T., 2026. Simple unilateral rupture of the great Mw 8.8 2025 Kamchatka earthquake. Science 391 (6787), 812–817. https://doi.org/10.1126/science.aeb8232.

MacInnes, B.T., Weiss, R., Bourgeois, J., Pinegina, T.K., 2010. Slip distribution of the 1952 Kamchatka great earthquake based on near-field tsunami deposits and historical records. Bull. Seismol. Soc. Am. 100 (4), 1695–1709. https://doi.org/10.1785/0120090376.

Manga, M., Brodsky, E.E., 2006. Seismic triggering of eruptions in the far field: volcanoes and geysers. Annu. Rev. Earth Planet Sci. 34, 263–291. https://doi.org/10.1146/annurev.earth.34.031405.125125.

Marsan, D., Helmstetter, A., Bouchon, M., Dublanchet, P., 2014. Foreshock activity related to enhanced aftershock production: foreshock and aftershock activities. Geophys. Res. Lett. 41 (19), 6652–6658. https://doi.org/10.1002/2014GL061219.

Martínez-Garzón, P., Poli, P., 2024. Cascade and pre-slip models oversimplify the complexity of earthquake preparation in nature. Commun. Earth Environ. 5, 120. https://doi.org/10.1038/s43247-024-01285-y.

McLaskey, G.C., 2019. Earthquake initiation from laboratory observations and implications for foreshocks. J. Geophys. Res. 124 (12), 12882–12904. https://doi.org/10.1029/2019JB018363.

Mecozzi, A., Antonelli, C., Marullo, A., Decaroli, D., Palmieri, L., Schenato, L., et al., 2025. Earth-scale precursors of the Kamchatka earthquake revealed via polarization monitoring in undersea Mediterranean optical fiber links. Optica. https://doi.org/10.1364/OPTICA.586317 accepted.

Mikhailov, V.O., Konvisar, A.M., Smirnov, V.B., Timoshkina, E.P., Titkov, N.N., Khairetdinov, S.A., Chebrov, D.V., 2025. The Rupture Surface Model of the July 29, 2025 Mw 8.8 Kamchatka Earthquake based on Satellite Geodesy and Interferometry Data. IDokl. Earth Sc 525, 35. https://doi.org/10.1134/S1028334X25608752.

Mousavi, S.M., Ellsworth, W.L., Zhu, W., Chuang, L.Y., Beroza, G.C., 2020. Earthquake transformer—an attentive deep-learning model for simultaneous earthquake detection and phase picking. Nat. Commun. 11 (1), 3952. https://doi.org/10.1038/s41467-020-17591-w.

Moutote, L., Itoh, Y., Lengliné, O., Duputel, Z., Socquet, A., 2023. Evidence of a transient aseismic slip driving the 2017 Valparaiso earthquake sequence, from foreshocks to aftershocks. J. Geophys. Res. Solid Earth 128, e2023JB026603. https://doi.org/10.1029/2023JB026603.

Nanjo, K.Z., Hirata, N., Obara, K., Kasahara, K., 2012. Decade-scale decrease in b value prior to the M9-class 2011 Tohoku and 2004 Sumatra quakes. Geophys. Res. Lett. 39, L20304. https://doi.org/10.1029/2012GL052997.

Neves, M., Chuang, L.Y., Li, W., et al., 2024. Complex rupture dynamics of the extremely shallow August 2020 M5.1 Sparta, North Carolina earthquake. Commun. Earth Environ. 5, 163. https://doi.org/10.1038/s43247-024-01316-8.

Noda, H., Nakatani, M., Hori, T., 2013. Large nucleation before large earthquakes is sometimes skipped due to cascade-up—Implications from a rate and state simulation of faults with hierarchical asperities. J. Geophys. Res. 118, 2924–2952. https://doi.org/10.1002/jgrb.50211.

Ogata, Y., 1988. Statistical models for earthquake occurrences and residual analysis for point processes. J. Am. Stat. Assoc. 83 (401), 9–27. https://doi.org/10.1080/01621459.1988.10478560.

Peng, Z., Lei, X., 2025. Physical mechanisms of earthquake nucleation and foreshock: cascade triggering, aseismic slip, or fluid flows? Earthq. Res. Adv. 5 (2), 100349. https://doi.org/10.1016/j.eqrea.2024.100349.

Peng, Z., Zhao, P., 2009. Migration of early aftershocks following the 2004 Parkfield earthquake. Nat. Geosci. 2 (12), 877–881. https://doi.org/10.1038/ngeo697.

Peng, Z., Vidale, J.E., Ishii, M., Helmstetter, A., 2007. Seismicity rate immediately before and after main shock rupture from high-frequency waveforms in Japan. J. Geophys. Res. Solid Earth 112, B03306. https://doi.org/10.1029/2006JB004386.

Peng, Z., Lei, X., Wang, Q.-Y., Wang, D., Mach, P., Yao, D., Kato, A., Obara, K., Campillo, M., 2025b. The evolution process between the earthquake swarm beneath the Noto Peninsula, central Japan and the 2024 M 7.6 Noto Hanto earthquake sequence. Earthq. Res. Adv. 5 (1), 100332. https://doi.org/10.1016/j.eqrea.2024.100332.

Peng, Z., Lei, X., Wang, D., Si, X., Mach, P., Zhong, Q., Ding, C., Deng, Y., Qin, M., Miao, S., 2025a. Mainshock rupture properties, aftershock activities and remotely triggered seismicity associated with the 2025 Mw 7.7 Sagaing fault earthquake in Myanmar. Earthq. Res. Adv. 5 (4), 100413. https://doi.org/10.1016/j.eqrea.2025.100413.

Perfettini, H., Avouac, J.-P., 2004. Postseismic relaxation driven by brittle creep: a possible mechanism to reconcile geodetic measurements and the decay rate of aftershocks, application to the Chi-Chi earthquake, Taiwan. J. Geophys. Res. Solid Earth 109, B02304. https://doi.org/10.1029/2003JB002488.

Perfettini, H., Avouac, J.-P., 2007. Modeling afterslip and aftershocks following the 1992 Landers earthquake. J. Geophys. Res. Solid Earth 112, B07409. https://doi.org/10.1029/2006JB004399.

Perfettini, H., Frank, W.B., Marsan, D., Bouchon, M., 2018. A model of aftershock migration driven by afterslip. Geophys. Res. Lett. 45, 2283–2293. https://doi.org/10.1002/2017GL076287.

Periollat, A., Funning, G., 2026. Linking Interseismic locking to Coseismic Rupture: the 2025 Mw 8.8 Kamchatka Earthquake. ESS Open Archive. https://doi.org/10.22541/essoar.176945501.18343723/v1.

Pinegina, T.K., Ozerov, A.Y., Tsvetkov, V.A., et al., 2026. Tsunami from the Mw 8.8 Kamchatka earthquake of 29 July 2025 on the east coast of Kamchatka and the North Kuril Islands. Pure Appl. Geophys. 183, 1–25. https://doi.org/10.1007/s00024-025-03873-1.

Rodkin, M.V., Irmak, T.S., Taymaz, T., Liperovskaya, E.V., 2025. Typical precursor anomalies of the February 6, 2023, Mw 7.8 and Mw 7.6 Kahramanmaraş earthquake doublet, Turkey, and the Mw 9.0+ Andaman-Sumatra and Tohoku, Japan mega-earthquakes. Izv. Phys. Solid Earth 61, 575–585. https://doi.org/10.1134/S1069351325700569.

Roeloffs, E., 2006. Evidence for aseismic deformation rate changes prior to earthquakes. Annu. Rev. Earth Planet Sci. 34, 591–627. https://doi.org/10.1146/annurev.earth.34.031405.124947.

Ross, Z.E., Rollins, C., Cochran, E.S., Hauksson, E., Avouac, J.-P., Ben-Zion, Y., 2017. Aftershocks driven by afterslip and fluid pressure sweeping through a fault-fracture mesh. Geophys. Res. Lett. 44, 8260–8267. https://doi.org/10.1002/2017GL074634.

Ross, Z.E., Idini, B., Jia, Z., Stephenson, O.L., Zhong, M., Wang, X., Zhan, Z., Simons, M., Fielding, E.J., Yun, S.-H., Hauksson, E., Moore, A.W., Liu, Z., Jung, J., 2019. Hierarchical interlocked orthogonal faulting in the 2019 Ridgecrest earthquake sequence. Science 366 (6463), 346–351. https://doi.org/10.1126/science.aaz0109.

Ruiz, S., Métois, M., Fuenzalida, A., Ruiz, J., Leyton, F., Grandin, R., Vigny, C., Madariaga, R., Campos, J., 2014. Intense foreshocks and a slow slip event preceded the 2014 Iquique Mw 8.1 earthquake. Science 345 (6201), 1165–1169. https://doi.org/10.1126/science.1256074.

Ruiz-Angulo, A., Melgar, D., de Marez, C., Deniau, A., Nencioli, F., Hjörleifsdóttir, V., 2025. SWOT satellite altimetry observations and source model for the tsunami from the 2025 Mw 8.8 Kamchatka earthquake. Seism. Rec. 5 (4), 341–351. https://doi.org/10.1785/0320250037.

Ruppert, N.A., Lees, J.M., Kozyreva, N.P., 2007. Seismicity, earthquakes and structure along the Alaska-Aleutian and Kamchatka-Kurile subduction zones: a review. In: Eichelberger, J., Gordeev, E., Izbekov, P., Kasahara, M., Lees, J. (Eds.), Volcanism and Subduction: the Kamchatka Region. https://doi.org/10.1029/172GM12.

Sawazaki, K., 2021. Early forecast of maximum amplitude due to aftershocks by applying extreme value statistics to a single continuous seismogram. Bull. Seismol. Soc. Am. 111 (5), 2825–2845. https://doi.org/10.1785/0120200365.

Schorlemmer, D., Wiemer, S., Wyss, M., 2005. Variations in earthquake-size distribution across different stress regimes. Nature 437, 539–542. https://doi.org/10.1038/nature04094.

Shapiro, S.A., Huenges, E., Borm, G., 1997. Estimating the crust permeability from fluid-injection-induced seismic emission at the KTB site. Geophys. J. Int. 131 (2), F15–F18. https://doi.org/10.1111/j.1365-246X.1997.tb01215.x.

Shcherbakov, R., Turcotte, D.L., 2004. A modified form of Båth's law. Bull. Seismol. Soc. Am. 94 (5), 1968–1975. https://doi.org/10.1785/012003162.

Shearer, P.M., Shakibay Senobari, N., 2025. Continuous aftershock hum for over ten days following the 2019 Ridgecrest, California, earthquakes observed with borehole seismometers. Seismol Res. Lett. 96 (5), 2968–2978. https://doi.org/10.1785/0220250017.

Shelly, D.R., 2024. Examining the connections between earthquake swarms, crustal fluids, and large earthquakes in the context of the 2020–2024 Noto Peninsula, Japan, earthquake sequence. Geophys. Res. Lett. 51, e2023GL107897. https://doi.org/10.1029/2023GL107897.

Sheng, Y., Mordret, A., Sager, K., Brenguier, F., Boué, P., Rousset, B., et al., 2022. Monitoring seismic velocity changes across the San Jacinto Fault using train-generated seismic tremors. Geophys. Res. Lett. 49, e2022GL098509. https://doi.org/10.1029/2022GL098509.

Shibata, R., Kubo, H., Suzuki, W., 2025. Source process of the 2025 Mw 8.8 Kamchatka Peninsula, Russia, earthquake revealed by back-projection and waveform inversion. ESS Open Archive. https://doi.org/10.22541/essoar.176536587.77974401/v1.

Stein, R.S., Toda, S., Lotto, G., Gonzalez-Huizar, H., Sevilgen, V., 2025. Huge July 2025 Kamchatka earthquake followed unusually productive foreshock sequence. Temblor. https://doi.org/10.32858/temblor.366.

Styron, R.H., Hetland, E.A., 2015. The weight of the mountains: constraints on tectonic stress, friction, and fluid pressure in the 2008 Wenchuan earthquake from estimates of topographic loading. J. Geophys. Res. 120 (4), 2697–2716. https://doi.org/10.1002/2014JB011338.

Tan, X., Yue, H., Liu, Y., Xu, X., Shi, F., Xu, C., Ren, Z., Shyu, J.B.H., Lu, R., Hao, H., 2018. Topographic loads modified by fluvial incision impact fault activity in the Longmenshan thrust belt, eastern margin of the Tibetan Plateau. Tectonics 37 (9), 3001–3017. https://doi.org/10.1029/2017TC004864.

Tarumi, K., Yoshizawa, K., 2025. Multi-frequency teleseismic P-wave back-projection of the 2025 Mw 8.8 Kamchatka Peninsula earthquake. Earth Planet Sci. Lett. https://doi.org/10.31223/X5S466 in review.

Tormann, T., Enescu, B., Woessner, J., et al., 2015. Randomness of megathrust earthquakes implied by rapid stress recovery after the Japan earthquake. Nat. Geosci. 8, 152–158. https://doi.org/10.1038/ngeo2343.

Utsu, T., Ogata, Y., Matsu'ura, R.S., 1995. The centenary of the Omori formula for a decay law of aftershock activity. J. Phys. Earth 43 (1), 1–33. https://doi.org/10.4294/jpe1952.43.1.

van der Elst, N.J., 2021. B-positive: a robust estimator of aftershock magnitude distribution in transiently incomplete catalogs. J. Geophys. Res. Solid Earth 126, e2020JB021027. https://doi.org/10.1029/2020JB021027.

Walter, T.R., Amelung, F., 2007. Volcanic eruptions following M $\geq$ 9 megathrust earthquakes: implications for the Sumatra-Andaman volcanoes. Geology 35 (6), 539–542. https://doi.org/10.1130/G23429A.1.

Wang, D., Mori, J., 2011. Rupture process of the 2011 off the Pacific coast of Tohoku earthquake (Mw 9.0) as imaged with back-projection of teleseismic P waves. Earth Planets Space 63, 603–607. https://doi.org/10.5047/eps.2011.05.029.

Wang, D., Kawakatsu, H., Mori, J., Ali, B., Ren, Z., Shen, X., 2016. Back-projection analyses from four regional arrays for rupture over a curved dipping fault: the Mw 7.7 September 24, 2013 Pakistan earthquake. J. Geophys. Res. Solid Earth 121 (3), 1948–1961. https://doi.org/10.1002/2015JB012168.

Wang, K., Huang, T., Tilmann, F., Peacock, S.M., Lange, D., 2020. Role of serpentinized mantle wedge in affecting megathrust seismogenic behavior in the area of the 2010 M 8.8 Maule earthquake. Geophys. Res. Lett. 47, e2020GL090482. https://doi.org/10.1029/2020GL090482.

Wang, K., Peng, Z., Liang, S., Luo, J., Zhang, K., He, C., 2024. Migrating foreshocks driven by a slow slip event before the 2021 MW 6.1 Yangbi, China earthquake. J. Geophys. Res. Solid Earth 129. https://doi.org/10.1029/2023JB027209 e2023JB027209.

Wang, K., Luo, H., He, J., Carvajal, M., 2025. Soft barrier to megathrust rupture enabled by serpentinized mantle wedge: the Chile subduction zone. Earth Planet Sci. Lett. 650, 119115. https://doi.org/10.1016/j.epsl.2024.119115.

Wetzler, N., Lay, T., Brodsky, E.E., 2023. Global characteristics of observable foreshocks for large earthquakes. Seismol Res. Lett. 94 (5), 2313–2325. https://doi.org/10.1785/0220220397.

Woessner, J., Wiemer, S., 2005. Assessing the quality of earthquake catalogues: estimating the magnitude of completeness and its uncertainty. Bull. Seismol. Soc. Am. 95, 684–698. https://doi.org/10.1785/0120040007.

Xu, D., Wang, W., Ren, Z., 2025. Preliminary slip distribution of the July 29, 2025 Mw 8.8 Kamchatka, Russia earthquake. Earthq. Res. Adv., 100427 https://doi.org/10.1016/j.eqrea.2025.100427.

Yagi, Y., Fukahata, Y., Okuwaki, R., Takagawa, T., Toda, S., 2025. Breaking the cycle: short recurrence and overshoot of an M9-class Kamchatka earthquake. Seismica 4 (2). https://doi.org/10.26443/seismica.v4i2.2012.

Yang, H., Zhu, L., Chu, R., 2009. Fault-plane determination of the 18 April 2008 Mount Carmel, Illinois, earthquake by detecting and relocating aftershocks. Bull. Seismol. Soc. Am. 99 (6), 3413–3420. https://doi.org/10.1785/0120090038.

Yin, H.Z., Allstadt, K., Barnhart, W.D., Clapp, S.A., Earle, P.S., Goldberg, Dara E., Grant, A.R.R., Herman, M.W., Jaiswal, K., McBride, S.K., et al., 2026. Rapid Characterization of the 2025 Mw 8.8 Kamchatka, Russia Earthquake. Seism. Rec. 6 (1), 1–12. https://doi.org/10.1785/0320250038.

Yu, C., Li, Z., Penna, N.T., Crippa, P., 2018. Generic atmospheric correction model for interferometric synthetic aperture radar observations. J. Geophys. Res. Solid Earth 123 (10), 9202–9222. https://doi.org/10.1029/2017JB015305.

Yue, H., Lu, W., Li, G., 2026. Post-foreshock transient slip in the 2016 Kumamoto sequence: a fourth foreshock mode. Earth Planet. Sci. Lett. 681, 119905. https://doi.org/10.1016/j.epsl.2026.119905.

Zhan, Z., Helmberger, D.V., Li, D., 2014. Imaging subducted slab structure beneath the Sea of Okhotsk with teleseismic waveforms. Phys. Earth Planet. Inter. 232, 30–35. https://doi.org/10.1016/j.pepi.2014.03.008.

Zhang, J., Kato, A., Wang, W., Zhang, M., 2025. Foreshock migration preceding the 2025 Mw 8.8 Kamchatka earthquake: insights from single-station observations. Geophys. Res. Lett. https://doi.org/10.1029/2025GL120956.

Zhou, Y., Ren, C., Ghosh, A., Meng, H., Fang, L., Yue, H., et al., 2022. Seismological characterization of the 2021 Yangbi foreshock-mainshock sequence, Yunnan, China: more than a triggered cascade. J. Geophys. Res. Solid Earth 127, e2022JB024534. https://doi.org/10.1029/2022JB024534.

Zhou, Y., Wang, W., Xu, D., Wang, X., Pan, Z., He, J., Yao, Z., 2025. Rupture and tectonic controls of the 2025 Mw 8.8 Kamchatka subduction earthquake in Far East Russia. Sci. Bull. https://doi.org/10.1016/j.scib.2025.12.005.

Ziv, A., 2003. Foreshocks, aftershocks, and remote triggering in quasi-static fault models. J. Geophys. Res. 108 (B10), 2498. https://doi.org/10.1029/2002JB002318.